The Architecture of the GW Ori Young Triple-star System and Its Disk: Dynamical Masses, Mutual Inclinations, and Recurrent Eclipses

Ian Czekala[1,12] , Sean M. Andrews[2] , Guillermo Torres[2] , Joseph E. Rodriguez[2] , Eric L. N. Jensen[3] , Keivan G. Stassun[4,5] ,
David W. Latham[2] , David J. Wilner[2] , Michael A. Gully-Santiago[6] , Konstantin N. Grankin[7] , Michael B. Lund[4] ,
Rudolf B. Kuhn[8] , Daniel J. Stevens[9] , Robert J. Siverd[10] , David James[2,13] , B. Scott Gaudi[9] , Benjamin J. Shappee[11,14] , and
Thomas W.-S. Holoien[11,15]

[1] Kavli Institute for Particle Astrophysics and Cosmology, Stanford University, 452 Lomita Mall, Stanford, CA 94305, USA; iczekala@stanford.edu
[2] Harvard-Smithsonian Center for Astrophysics, 60 Garden Street, Cambridge, MA 02138, USA
[3] Department of Physics and Astronomy, Swarthmore College, 500 College Avenue, Swarthmore, PA 19081, USA
[4] Department of Physics and Astronomy, Vanderbilt University, 6301 Stevenson Center, Nashville, TN 37235, USA
[5] Department of Physics, Fisk University, Nashville, TN 37208, USA
[6] NASA Ames Research Center, Moffett Field, CA 94035, USA
[7] Crimean Astrophysical Observatory, pos. Nauchnyi, Crimea, 298409, Russia
[8] South African Astronomical Observatory, P.O. Box 9, Observatory 7935, South Africa
[9] Department of Astronomy, The Ohio State University, Columbus, OH 43210, USA
[10] Las Cumbres Observatory Global Telescope Network, 6740 Cortona Drive, Suite 102, Santa Barbara, CA 93117, USA
[11] The Observatories of the Carnegie Institution for Science, 813 Santa Barbara Street, Pasadena, CA 91101, USA

Abstract

We present spatially and spectrally resolved Atacama Large Millimeter/submillimeter Array (ALMA) observations of gas and dust orbiting the pre-main-sequence hierarchical triple-star system GW Ori. A forward modeling of the ^{13}CO and C^{18}O $J = 2$–1 transitions permits a measurement of the total stellar mass in this system, $5.29 \pm 0.09\,M_{\odot}$, and the circumtriple disk inclination, $137°.6 \pm 2°.0$. Optical spectra spanning a 35 yr period were used to derive new radial velocities and, coupled with a spectroscopic disentangling technique, revealed that the A and B components of GW Ori form a double-lined spectroscopic binary with a period of 241.50 ± 0.05 days; a tertiary companion orbits that inner pair with a period of 4218 ± 50 days. Combining the results from the ALMA data and the optical spectra with three epochs of astrometry in the literature, we constrain the individual stellar masses in the system ($M_{\rm A} \approx 2.7\,M_{\odot}$, $M_{\rm B} \approx 1.7\,M_{\odot}$, $M_{\rm C} \approx 0.9\,M_{\odot}$) and find strong evidence that at least one of the stellar orbital planes (and likely both) is misaligned with the disk plane by as much as $45°$. A V-band light curve spanning 30 yr reveals several new $\sim$30-day eclipse events 0.1–0.7 mag in depth and a 0.2 mag sinusoidal oscillation that is clearly phased with the AB–C orbital period. Taken together, these features suggest that the A–B pair may be partially obscured by material in the inner disk as the pair approaches apoastron in the hierarchical orbit. Lastly, we conclude that stellar evolutionary models are consistent with our measurements of the masses and basic photospheric properties if the GW Ori system is $\sim$1 Myr old.

Key words: protoplanetary disks – stars: fundamental parameters – stars: individual (GW Ori) – stars: pre-main sequence

Supporting material: machine-readable tables

1. Introduction

Pre-main-sequence (PMS) stars in multiple systems—for which it is possible to precisely measure their fundamental stellar properties through dynamical means—serve as touchstones for understanding the final stages of stellar formation and the conditions under which planetary systems are assembled. While recent decades have seen steady progress in understanding binary formation in general, lingering uncertainties still remain about the characteristics of young spectroscopic binaries and higher-order systems (Duchêne & Kraus 2013).

GW Ori, a G-type star associated with the λ Orionis OB star-forming complex (Dolan 2000; Dolan & Mathieu 2001, 2002), was one of the first T Tauri stars to be revealed as a spectroscopic binary, with a period of 240 days (Mathieu et al. 1991). Radial velocity (RV) monitoring hinted at the presence of a third body with a period of ∼10 yr; a tertiary was confirmed directly using infrared interferometry (Berger et al. 2011). Circumstellar material in the GW Ori system was first inferred from infrared excess emission (Mathieu et al. 1991); a subsequent detection of the dust continuum at submillimeter wavelengths suggested that the disk was especially massive and must be circumbinary ($M_{\rm disk} \gtrsim 0.1 M_{\odot}$; Mathieu et al. 1995).

The disk material provided a natural explanation for the quasi-periodic optical dimming of GW Ori over ∼30-day durations: the suspicion was that a disk around the secondary was eclipsing the primary, presuming a nearly edge-on viewing angle (Shevchenko et al. 1992, 1998). Fang et al. (2017) spatially resolved the disk material with Submillimeter Array (SMA) observations of the dust continuum and the line emission from CO isotopologues, demonstrating its large radial extent and therefore presumably circumtriple architecture. However, they found that the disk has an *intermediate* inclination to the line of sight ($i_{\rm disk} \approx 35°$), in apparent conflict

---

[12] KIPAC Postdoctoral Fellow.
[13] Event Horizon Telescope.
[14] Hubble, Carnegie-Princeton Fellow.
[15] Carnegie Fellow.

with the eclipse model. Indeed, this adds to a collection of indirect evidence for a more complicated geometry in the inner disk, including mid-infrared fluxes that vary on ~ 1 yr timescales (Fang et al. 2014) and CO rovibrational emission lines with multicomponent profiles (which requires a complicated geometry and/or temperature structure in the inner disk; Najita et al. 2003).

Beyond resolving outstanding questions about its architecture, the GW Ori system presents an excellent opportunity to obtain a precise dynamical mass measurement for an earlier-type ($\sim$G8) star at a very young age. Precise dynamical masses are crucial for calibrating the photospheric predictions (e.g., T_{eff}, L) of stellar evolutionary models, and the region of the Hertzsprung–Russell (H-R) diagram occupied by GW Ori is particularly sparsely populated with benchmark systems (Stassun et al. 2014). Especially interesting is the fact that three different dynamical mass measurement techniques can be employed to study the GW Ori system: (1) RV monitoring, which constrains the mass ratios of the stars (Mathieu et al. 1991; Fang et al. 2014); (2) astrometric monitoring, which provides the inclinations of the orbits and, when coupled with RV measurements, can reveal the individual component masses (Berger et al. 2011); and (3) the disk-based dynamical mass technique (e.g., Simon et al. 2000, 2017; Rosenfeld et al. 2012; Czekala et al. 2015a, 2016), which measures the *total* stellar mass.

In this paper, we combine information from each of these techniques to better understand the fundamental properties and underlying physical architecture of the GW Ori system. Section 2 describes new ALMA observations of the GW Ori disk, an updated analysis of 35 yr of optical spectroscopic RV monitoring, and an extensive decades-long optical photometric catalog. Section 3 describes our tomographic reconstruction of the disk velocity field, a new analysis of the RV data, their combination with literature-based astrometric constraints (Berger et al. 2011), an assessment of the system parameters and geometry, and the connections to the observed photometric variations. Section 4 concludes by discussing the structure and orientation of the disk with respect to the orbital architecture of the triple system and considers the GW Ori system in the context of other young multiple PMS systems.

2. Observations and Data Reduction

2.1. Millimeter Interferometry

GW Ori was observed with the ALMA interferometer on 2015 May 14 (program ID 2012.1.00496.S), with 37 of the 12 m main array antennas configured to span baselines of 23–558 m. The double-sideband Band 6 receivers were employed in dual-polarization mode, and the ALMA correlator was set up to process data in four spectral windows (SPWs). Two of these SPWs, centered at 220.426 and 230.450 GHz to observe the ^{13}CO and ^{12}CO $J = 2$–1 transitions (at rest frequencies of 220.399 and 230.538 GHz, respectively), covered 234 MHz of bandwidth in 3840 channels (a 61 kHz channel spacing). One other sampled 469 MHz around 219.763 GHz to observe the C^{18}O $J = 2$–1 transition (at rest frequency 219.560 GHz) with 3840 channels (a 122 kHz channel spacing). The last SPW sampled the continuum in a 1.875 GHz range around 231.956 GHz using 128 coarse channels (a 15.625 MHz channel spacing).

Table 1
ALMA Image Properties

|	Beam Dimensions	rms (mJy beam^{-1})
226 GHz continuum	$0.''88 \times 0.''54$, 126°	0.055
^{12}CO $J = 2$−1	$0.''89 \times 0.''56$, 126°	6
^{13}CO $J = 2$−1	$0.''93 \times 0.''59$, 126°	8
C^{18}O $J = 2$−1	$0.''92 \times 0.''58$, 126°	5

Note. The rms noise levels recorded for the spectral line cubes correspond to the values per 170 m s^{-1} channel.

The observations cycled between GW Ori and the quasar J0510+1800 with a 7-minute cadence. The quasar J0423 −0120 and Ganymede were observed as bandpass and flux calibration sources, respectively, at the start of the execution block. The total on-source integration time for GW Ori was 16 minutes. The observing conditions were typical for Band 6 projects, with a precipitable water vapor level around 1.1 mm.

The visibility data were calibrated with standard procedures using the CASA software package (v4.4). The raw, observed visibility phases were adjusted based on the contemporaneous measurements of water vapor radiometers and flagged when applicable, and then the bandpass shape in each SPW was calibrated based on the observations of J0423−0120. The absolute amplitude scale was determined based on the observations of Ganymede. The complex gain behavior of the array and atmosphere was corrected based on the repeated observations of J0510+1800. The calibrated visibilities showed a strong continuum signal, suggesting that self-calibration could significantly improve the data quality. An initial model based on a preliminary continuum image was used for two rounds of phase-only self-calibration (on 30 s and then 6 s intervals) and one additional round that included the amplitudes (on a 7-minute scan interval). This self-calibration reduced the rms noise level in the continuum by a factor of $\sim$40. After applying the self-calibration tables to the entire data set (channel by channel), we parsed out data products for each individual emission tracer of interest. A set of continuum visibilities was constructed by spectrally averaging the line-free channels in each SPW into $\sim$125 MHz increments. The spectral visibilities for the ^{12}CO, ^{13}CO, and C^{18}O lines were continuum-subtracted and regridded into 170 m s^{-1} wide channels in the LSRK rest frame over a $\sim$10 km s^{-1} range around the line centers.

These fully reduced visibility sets were then imaged by Fourier inversion assuming a Briggs (robust = 0.5) weighting scheme and deconvolution with the standard CLEAN algorithm. Some basic image properties for the synthesized continuum image and spectral line image cubes are listed in Table 1. The continuum and spectral line moment maps are shown together in Figure 1, along with a comparison of the integrated spectra. The channel maps for individual lines are compiled in Figure 2.

The 226 GHz (1.3 mm) continuum map shows a bright (flux density = 202 ± 20 mJy), compact but marginally resolved (deconvolved Gaussian FWHM $\approx 0.''9$) source centered on the GW Ori stellar system, with a peak intensity of 67 mJy beam^{-1} (S/N $\approx$1200). Our integrated flux density measurement is consistent with that of Mathieu et al. (1925; 255 ± 60 mJy), but marginally discrepant with that of Fang et al. (2017; 320 ± 64 mJy). A crude estimate of the emission geometry (from a Gaussian fit to the visibilities) suggests an
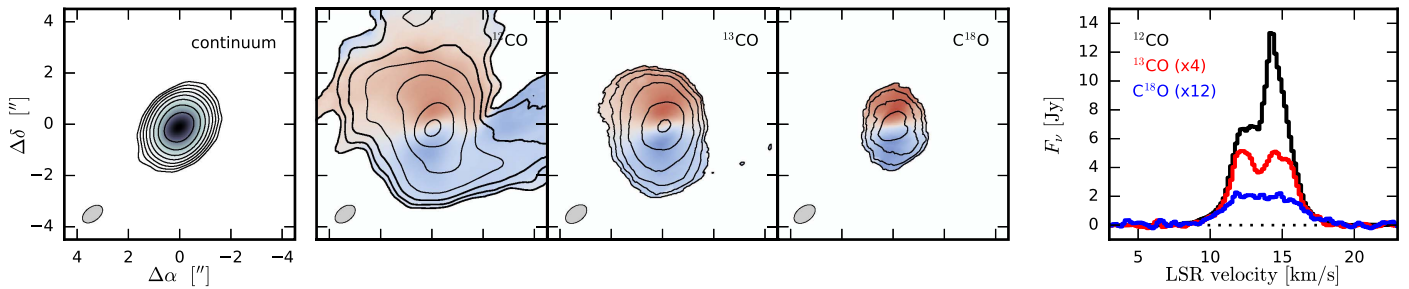
Figure 1. Left: 226 GHz continuum image. Contours start at 5× the rms noise level and increase by factors of 2. The synthesized beam geometry is shown in the lower left corner. Middle, left to right: maps of the ^{12}CO, ^{13}CO, and $C^{18}O$ velocity-integrated intensities (contours, starting at 10, 3, and 3× the rms noise levels, respectively, and increasing by factors of 2) overlaid on the intensity-weighted projected velocities (color scale). Note the prominent molecular cloud contamination in the ^{12}CO map (see also Figure 2). Right: spatially integrated spectra (inside the same CLEAN mask, and smoothed with a 0.85 km s^{-1} Hanning kernel) for each CO line.

inclination of 35°–40°, with the major axis oriented ∼170° E of N.

The CO isotopologue channel maps reveal bright (integrated intensities of 41.8, 5.7, and 0.8 Jy km s^{-1} for ^{12}CO, ^{13}CO, and $C^{18}O$, respectively) and extended (FWHM ∼2″.5) emission that is clearly in rotation around the continuum centroid, spanning a projected velocity range of ±5 km s^{-1} from the line center. The line emission is blueshifted to the south and redshifted to the north, consistent with the orientation estimated from the continuum emission. The peak intensities for each line are ∼800, 290, and 55 mJy beam^{-1} in the brightest channels (peak S/N ≈ 130, 35, and 14) for ^{12}CO, ^{13}CO, and $C^{18}O$, respectively. The ^{12}CO channel maps show some clear evidence for structured contamination from the surrounding molecular cloud, particularly as a streamer to the west at ∼11–13 km s^{-1} and some diffuse clumps to the north around 13–14 km s^{-1}, confirming the "tail"-like feature seen by Fang et al. (2017). These structures are much fainter, but still present, in ^{13}CO emission; they are not apparent in the $C^{18}O$ maps.

2.2. Optical Spectroscopy

GW Ori was monitored spectroscopically at the Harvard-Smithsonian Center for Astrophysics for more than 35 yr, beginning in 1981 November. A total of 203 usable spectra were gathered through 2009 April using three nearly identical echelle spectrographs (Digital Speedometers, DS; now decommissioned) with a resolving power of $R \approx$ 35,000 mounted on three different telescopes: the 1.5 m Tillinghast reflector at the Fred L. Whipple Observatory (Mount Hopkins, AZ), the 4.5 m equivalent Multiple Mirror Telescope (also on Mount Hopkins) before conversion to a monolithic mirror, and occasionally on the 1.5 m Wyeth reflector at the Oak Ridge Observatory (in the town of Harvard, MA). Each instrument was equipped with an intensified photon-counting Reticon detector limiting the output to a single echelle order 45 Å wide, which was centered on the region of the Mg I b triplet at 5187 Å (see Latham 1992). The signal-to-noise ratios (S/Ns) of these observations range from 14 to 59 per resolution element of 8.5 km s^{-1}, with a median of 41. Wavelength calibrations were based on exposures of a thorium-argon lamp taken before and after each science exposure. Reductions were performed with a dedicated pipeline, and the zero-point of the velocities was monitored regularly by means of exposures of the evening and morning twilight sky. The original analysis of Mathieu et al. (1991) used a subset of 45 of these spectra. A further 79 usable spectra of GW Ori were collected with the Tillinghast Reflector Echelle

Spectrograph (TRES; Fűrész 2008), a bench-mounted, fiber-fed echelle instrument attached to the 1.5 m Tillinghast reflector. It provides a resolving power of $R \approx$ 44,000, delivering 51 orders covering the wavelength interval 3900–9100 Å. These observations were made between 2010 November and 2017 April. S/Ns at 5200 Å range from 28 to 195 per resolution element of 6.8 km s^{-1}, with a median of 74. Wavelength calibration was carried out as above, and reductions were performed as described by Buchhave et al. (2010). RV standard stars were observed each night to monitor the zero-point and place it on the same system as the DS observations to within ∼0.1 km s^{-1}.

All of our spectra appear to be single-lined, with broad features indicative of significant rotation. Preliminary RV measurements were therefore made with standard 1D cross-correlation techniques, as in the analysis of Mathieu et al. (1991). However, several pieces of evidence suggested that it should be possible to detect the lines of the secondary in the 240-day binary. In particular, the large flux ratio of $f_B/f_A = 0.57 \pm 0.05$ (weighted average) reported by Berger et al. (2011) in the H band, when translated to the optical, would still be significant for any reasonable assumption of the effective temperatures, making our nondetection of the secondary somewhat surprising. Furthermore, those same authors proposed that the system is observed nearly face-on, which would lead to strong line blending that could explain our lack of detection despite the sizable brightness of the secondary.

We embarked on a search for such a signature using the then-under-development PSOAP spectroscopic disentangling package (Czekala et al. 2017), with the assumption that it must be at or near the detection limit (e.g., $q_{in} \lesssim 0.2$) since it had not been previously seen. Given a time series of high-resolution spectroscopic observations covering the orbital phase of the binary or triple star, PSOAP simultaneously infers the intrinsic spectrum of each star along with the stellar orbit using Gaussian processes as a modeling basis. This provides a robust probabilistic inference of both the orbits and spectra in a purely data-driven manner, which can further be used to measure fundamental properties with traditional analysis techniques. Preliminary results hinted at the detection of the secondary, but for mass ratios much larger than expected ($q_{in} > 0.5$). Because the algorithm was not yet fully vetted, we discounted those results. To our excitement, however, shortly thereafter we learned that GW Ori had been revealed as a *double*-lined binary based on high-resolution infrared spectroscopy ($q_{in} \sim 0.55$; Prato et al. 2017). Motivated by that result, we renewed our
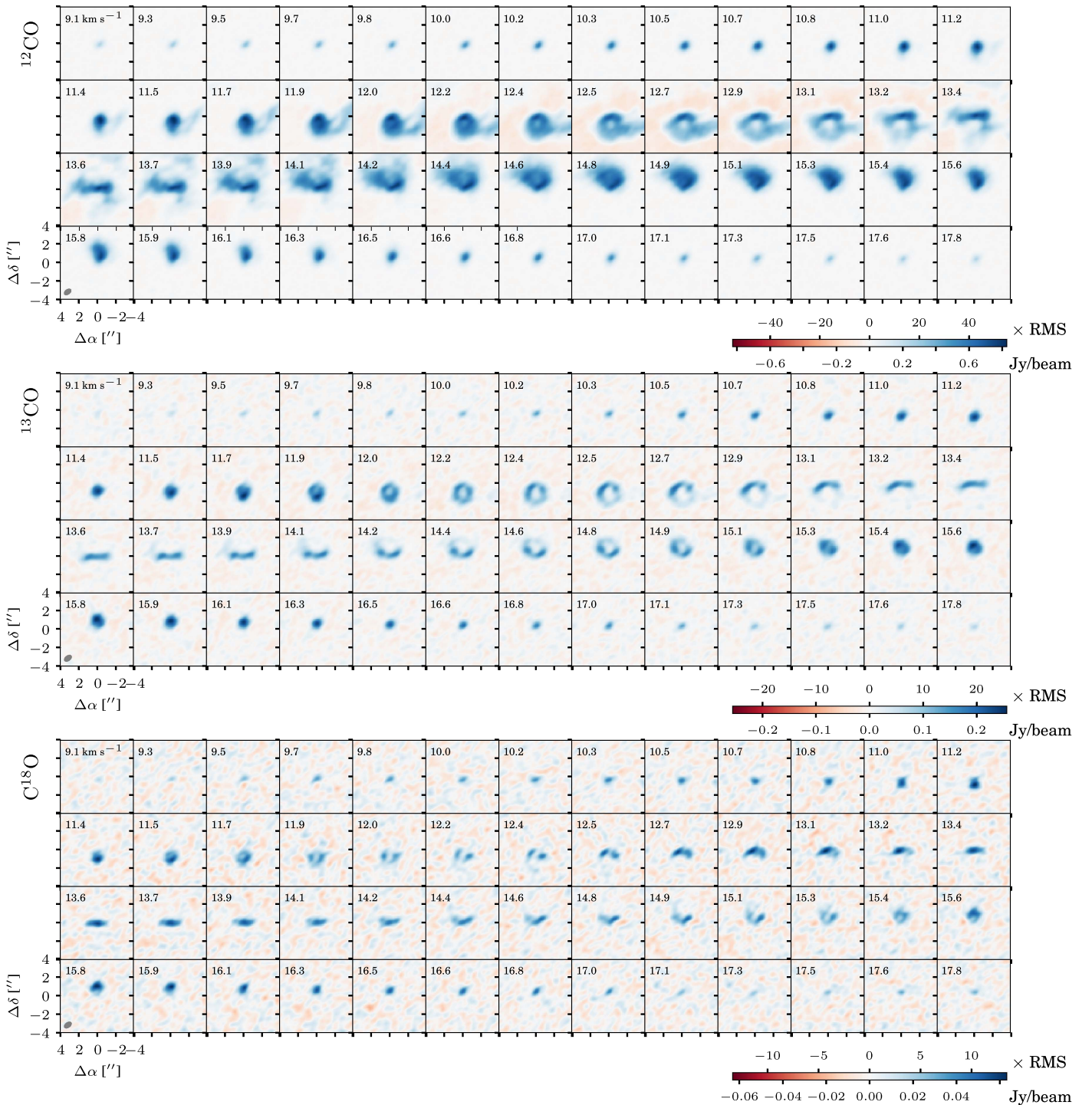
Figure 2. Channel maps of the ^{12}CO, ^{13}CO, and C^{18}O (from top to bottom) line emission from the GW Ori disk. Each channel represents the emission in a 170 m s^{-1} wide velocity bin. LSRK velocities are indicated in the upper left and synthesized beam sizes in the lower left of each panel. Scale bars are provided at the bottom right of each set of channel maps.

efforts to search for the secondary using PSOAP and a targeted TODCOR analysis, which is a 2D cross-correlation algorithm designed to minimize biases in the RVs due to line blending.

At present, one limitation of the PSOAP framework (and Gaussian processes in general, to some extent) is the extreme computational expense in performing large matrix calculations. This generally limits us to considering fewer than 20 epochs of high-resolution spectra at a time, which consequently limits

the complexity of the orbital model that can be used. Although it was straightforward to extend the framework to utilize a hierarchical triple orbital model and three Gaussian process components, we found that we were unable to employ enough spectroscopic epochs to sufficiently constrain the more complex orbital model. Therefore, we experimented using different subsets of the highest-S/N data in the range of 5060–5290 Å to test our sensitivity to the presence of the

Table 2
Heliocentric RV Measurements of GW Ori

HJD (2,400,000+)	RV_A (km s^{-1})	σ_A (km s^{-1})	RV_B (km s^{-1})	σ_B (km s^{-1})
44,919.0042	31.24	5.40	28.50	19.13
45,301.8865	25.10	5.18	25.29	18.35
45,336.7941	23.46	3.36	20.37	11.92
45,708.7038	33.05	5.83	20.37	20.65
45,709.6058	37.70	2.76	25.18	9.77

Note. Observations up to HJD 2,454,926.6573 were obtained with the DS, and the remainder with TRES.

(This table is available in its entirety in machine-readable form.)

secondary and tertiary spectral signatures. In all of these tests, we clearly detected the features of the secondary but found no obvious evidence for spectroscopic signatures of the tertiary.

Based on the guidance from these results, we reexamined our spectra with TODCOR and succeeded in detecting the secondary via cross-correlation, as well. As anticipated, the lines of the two stars are always heavily blended, which causes a strong degeneracy between the adopted rotational line broadening for the templates (see below), the velocity amplitudes, the adopted temperatures, and the flux ratio. To measure RVs, we adopted synthetic templates from the PHOENIX library of Husser et al. (2013), broadened to match the resolution of our spectra. For the TRES observations we restricted our analysis to the 100 Å order centered on the Mg I b triplet, both for consistency with the analysis of the DS spectra, which cover only a 45 Å window centered on this region, and because experience shows that it contains most of the information on the velocities. The 1D cross-correlations needed to construct the 2D correlation function in TODCOR were computed using the IRAF[16] task XCSAO (Kurtz & Mink 1998). The template parameters were selected based on an analysis of the stronger TRES spectra, as follows. For the primary star we adopted a temperature of $T_{eff} = 5700$ K proposed by Mathieu et al. (1991), along with $\log g = 3.0$ and solar metallicity, although the latter has minimal effect. The same composition and surface gravity were used for the secondary. The rotational broadening ($v \sin i$) of the primary, the secondary temperature, and the secondary $v \sin i$ were then determined by running extensive grids of 2D cross-correlations over broad ranges in each parameter in a manner similar to that described by Torres et al. (2002), seeking the best match between the templates and the observed spectra as measured by the peak cross-correlation coefficient averaged over all exposures. For each combination of template parameters we also determined the flux ratio that maximizes the correlation.

In this way we determined a best-fit secondary temperature of $T_{eff} = 4800 \pm 200$ K and $v \sin i$ values for the primary and secondary of 40 and 45 km s^{-1}, respectively, with estimated uncertainties of 5 km s^{-1}. The measured flux ratio in the Mg I b $\lambda 5187$ region is $f_B/f_A = 0.25 \pm 0.05$. While in principle these temperatures and $v \sin i$ values are merely free parameters that provide the best match to the observed spectra, in the following we interpret them also as estimates of the physical properties of

the stars. The RVs we measured from our DS and TRES spectra with these parameters are reported in Table 2, along with their uncertainties. Typical errors for the primary and secondary are 1.0 and 2.7 km s^{-1} for TRES and 2.5 and 8.7 km s^{-1} for the DS measurements, though individual errors can sometimes be much larger. Despite the use of TODCOR, we reiterate that the severe line blending at all phases of the inner orbit caused by a combination of rotational broadening and small velocity amplitudes makes the RVs very susceptible to errors in the template parameters (particularly $v \sin i$) and in the adopted flux ratio, and as a result the orbital elements presented later may suffer from systematic errors not included in the statistical uncertainties. Nevertheless, as a consistency check we used PHOENIX spectra from Husser et al. (2013) for the primary and secondary stellar parameters given above to extrapolate our measured flux ratio at 5187 Å to the near-infrared and obtained an H-band value of $f_B/f_A = 0.57 \pm 0.12$. While less precise than the Berger et al. (2011) measurement, the agreement is excellent.

2.3. Time-series Photometry

We have assembled a high-cadence light curve of GW Ori covering a ~30 yr time span by drawing from several ongoing photometric surveys and archival observations. The details of the different surveys used in compiling this catalog are described below.

2.3.1. Maidanak Observatory

Photoelectric *UBVR* observations of GW Ori were obtained at Mount Maidanak Observatory in Uzbekistan. About 530 *UBVR* magnitudes were collected from 1987 to 2003, although the number of *U* measurements is relatively small compared to the other photometric bands. All observations were performed with three telescopes (one 0.48 m and two 0.6 m reflectors) using identical single-channel pulse-counting photometers with FEU-79 photomultiplier tubes. The observations of GW Ori were carried out as part of the ROTOR program, which was described by Shevchenko et al. (1993).

The rms uncertainty for a single measurement in the instrumental system was 0.01 mag in *BVR* and 0.02 mag in *U*. Observations were carried out either differentially using a nearby reference star or directly by estimating the nightly extinction. In the latter case, several reference stars were observed every night to derive the extinction coefficients in each filter. Selected standard stars were observed and used to calibrate instrumental magnitudes on the Cousins system. We then transformed the magnitudes to the Johnson *UBVR* system using the relationship $(V - R)_C = -0.0320 + 0.71652(V - R)_J$. The systematic uncertainty in this conversion is 0.01 mag.

2.3.2. KELT

The Kilodegree Extremely Little Telescope (KELT) project uses two telescopes to survey over 70% of the entire sky searching for transiting planets around bright stars ($8 < V < 11$). The telescopes, located in Sonoita, Arizona (KELT-North), and Sutherland, South Africa (KELT-South), have a 42 mm Mamiya 645-series wide-angle lens resulting in a $26° \times 26°$ field of view (FOV) and a 23″ pixel scale. Both telescopes use a broad *R*-band filter. KELT observes using a Paramount ME German equatorial mount with a 180° meridian flip; therefore, KELT observes in either an "east" or "west" orientation. The telescope optics are not perfectly axisymmetric, and so the point-spread function (PSF)

---

[16] IRAF is distributed by the National Optical Astronomy Observatories, which are operated by the Association of Universities for Research in Astronomy, Inc., under cooperative agreement with the National Science Foundation.

Table 3
Photometric Measurements of GW Ori

HJD (2,400,000+)	m_V (mag)	σ_V (mag)	Telescope
47,031.4670	9.94	⋯	Maidanak
47,032.4760	9.90	⋯	Maidanak
47,034.4826	9.86	⋯	Maidanak
47,035.4806	9.88	⋯	Maidanak
47,036.4839	9.87	⋯	Maidanak

(This table is available in its entirety in machine-readable form.)

changes from one orientation to the other. Throughout the data reduction process, the east and west observations are treated as though they were acquired from separate telescopes. For GW Ori specifically, the PSF asymmetry results in a 0.2 mag systematic offset between the east and west orientations. See Siverd et al. (2012) and Kuhn et al. (2016) for a detailed description of the KELT observing strategy and reduction process. GW Ori was located in KELT-South field 05 ($\alpha = 06$ hr 07 m 48.0 s, $\delta = +3°00'00''$) and was observed 2889 times from UT 2010 February 28 until UT 2015 April 09, with a median uncertainty of 0.005 mag.

2.3.3. All-sky Automated Survey (ASAS)

Using two observing locations, in Las Campanas, Chile, and Haleakala, Maui, the ASAS project was designed to observe the entire sky to a limiting optical magnitude of 14. The two observatory setups each contained a wide-field Minolta 200/2.8 APO-G telephoto lenses with a 2K × 2K Apogee CCD and both observed simultaneously in B and V band. The telescope and camera setup correspond to an $8°8 \times 8°8$ FOV. ASAS observed GW Ori in the V band from UT 2001 March 11 until UT 2009 November 29, obtaining 480 observations with a median per-point uncertainty of 0.036 mag.

2.3.4. All-sky Automated Survey for Supernovae (ASAS-SN)

Focused on the discovery and characterization of supernovae, the ASAS-SN (Shappee et al. 2014; Kochanek et al. 2017) surveys the entire sky down to $V \sim 17$ mag every ~ 2 days. Hosted by the Las Cumbres Observatory at Mount Haleakala, Hawaii, and the Cerro Tololo Inter-American Observatory in Chile, each location hosts four 14 cm Nikon telephoto lenses with a 2K × 2K thinned CCD (Brown et al. 2013). The telescopes have a $4°5 \times 4°5$ FOV and a $7''8$ pixel scale. ASAS-SN obtained 799 observations of GW Ori from UT 2014 December 16 until UT 2017 March 15, with a typical per-point error of 0.01 mag. Table 3 lists all of the photometric observations from the aforementioned telescopes.

3. Analysis and Results

These new data sets allow us to study the architecture of the GW Ori system in a comprehensive manner. First, we forward-model the ALMA ^{13}CO and C^{18}O transitions to reconstruct the disk velocity field, measure its inclination, and determine the total stellar mass of GW Ori. Next, we fit a hierarchical triple-star model to the RVs and archival astrometry to determine individual stellar masses and orbital inclinations, and we compare these properties with those of the disk. Last, we use the extensive light curve of GW Ori to identify new eclipse events and oscillatory modes and compare these with the orbital periods to inform theories of their physical origin.

3.1. A Reconstruction of the Disk Velocity Field

We use the spatially and spectrally resolved molecular line emission observed with ALMA to tomographically reconstruct the disk velocity field and make a dynamical measurement of the total stellar mass in the GW Ori system. We follow the forward-modeling procedures described by Czekala et al. (2015a, 2016) using the associated open-source software package DiskJockey.[17]

The basis of the parametric physical model adopted in this approach is a radial surface density profile, $\Sigma(r)$, designed to mimic a simple theoretical description for a viscous accretion disk (Lynden-Bell & Pringle 1974; Hartmann et al. 1998). That profile decreases like $1/r$ interior to a characteristic radius R_c and has an exponential taper e^{-r/R_c} at larger radii. The vertical distribution of density is controlled by the temperature structure: we assume a vertically isothermal model with a radial profile $T(r) = T_{10}(r/10 \text{ au })^{-q}$. To convert the total gas densities to the volume density of a given species, we use abundance ratios that are representative of the dense interstellar medium: [H_2/gas] = 0.8, [H/H_2] = 2, [^{12}CO/H] = 7.5 ×10^{-5}, [^{12}CO/^{13}CO] = 69, and [^{12}CO/C^{18}O] = 557 (e.g., Henkel et al. 1994; Prantzos et al. 1996).

The disk kinematics are assumed to be Keplerian and dominated by the total stellar mass M_{tot}, with a velocity field that appropriately accounts for the 2D distribution of the emitting layer (see Rosenfeld et al. 2013). The line-spread function is characterized with a width defined by the quadrature sum of thermal and nonthermal (ξ; presumably turbulent) contributions. For any physical structure specified by these six parameters, $\{\Sigma_c, R_c, T_{10}, q, M_{tot}, \xi\}$, we solve the molecular rate equations (assuming LTE) and ray-trace the associated emission into a set of high-resolution channel maps using the radiative transfer package RADMC-3D (Dullemond 2012). That ray tracing requires that we specify five additional geometric parameters: the disk inclination to the line of sight (i_{disk}), the position angle of the disk rotation axis projected on the sky (φ), the LSRK systemic RV (v_r), and a pair of positional offsets from the observed pointing (μ_α, μ_δ). We adopt a fixed distance to the GW Ori system, $d = 388$ pc (Kounkel et al. 2017), to make the problem more computationally tractable; the effects of this assumption are discussed in Section 3.3. The *Gaia* DR1 parallax to GW Ori is still rather uncertain: the mean estimate is slightly larger than our adopted distance, but its large uncertainty means that it is still consistent at the 1σ level ($\pi = 2.1 \pm 0.5$ mas; Gaia Collaboration et al. 2016).

The model channel maps are then Fourier-transformed and sampled at the same spatial frequencies observed by ALMA. The model quality with respect to the observed visibilities is evaluated with a χ^2 likelihood function that incorporates the nominal visibility weights. We assume flat priors on all parameters except for i_{disk}, where instead we adopt a simple geometric prior (the disk angular momentum vector is distributed uniformly on a sphere; e.g., Czekala et al. 2016). The posterior distribution of these parameters is explored using Markov Chain Monte Carlo (MCMC) simulations with the affine invariant ensemble sampler proposed by Goodman & Weare (2010), as implemented in the emcee code

---

[17] Available under an MIT license at https://github.com/iancze/DiskJockey.

Table 4
Inferred Disk Model Parameters

Parameter	^{13}CO	C^{18}O
$M_{\rm tot}\,(M_\odot)$	5.28 ± 0.06	5.38 ± 0.23
r_c (au)	237 ± 5	151 ± 21
T_{10} (K)	51 ± 2	32 ± 4
q	0.308 ± 0.012	0.378 ± 0.037
$\log_{10} M_{\rm disk}\,\log_{10}(M_\odot)$	-1.69 ± 0.02	-1.02 ± 0.22
ξ (km s^{-1})	0.59 ± 0.01	0.37 ± 0.03
i_d (deg)	137.7 ± 0.3	135.2 ± 1.4
PA[a] (deg)	90.7 ± 0.1	90.5 ± 0.6
v_r[b] (km s^{-1})	$+13.651 \pm 0.003$	$+13.649 \pm 0.015$
μ_α ($''$ yr^{-1})	-0.004 ± 0.002	-0.028 ± 0.010
μ_δ ($''$ yr^{-1})	-0.044 ± 0.002	-0.051 ± 0.008

Notes. The 1D marginal posteriors are well described by a Gaussian, so we report symmetric error bars here.
[a] For comparison with the stellar orbits, we note that the position angle of the ascending node $\Omega_{\rm disk}$ is 90° offset from our PA convention, i.e., $\Omega_{\rm disk} = {\rm PA} + 90° \approx 180°.6$.
[b] LSRK reference frame. In the barycentric reference frame, the disk systemic velocity is $+28.34$ km s^{-1}.

(Foreman-Mackey et al. 2013) and ported to the Julia programming language (included in DiskJockey).

Compared to previous similar work, the modeling of GW Ori is considerably more computationally expensive. This is primarily a consequence of the large physical size of the disk, which makes the ray-tracing step substantially more time-consuming. The inference for an individual spectral line takes ~10,000 CPU hours parallelized across 26 cores on the Harvard Odyssey cluster. Given that expense and the fact that the ^{12}CO line is clearly contaminated by local cloud material, we restrict our analysis to *independent* inferences of the model parameters based on the ^{13}CO and C^{18}O data sets. For expediency, we only model the data averaged to 25 channels of 0.4 km s^{-1} width. Experiments modeling a subset of the channels at higher resolution (e.g., using every third 0.17 km s^{-1} wide channel) yielded similar results.

The parameter values inferred from each spectral line data set are summarized together in Table 4. A comparison of the data and the best-fit models (and associated residuals) is presented in the form of channel maps in Figures 3 and 4 for ^{13}CO and C^{18}O, respectively. While overall the models successfully reproduce the observed emission, there are some interesting residuals, namely, an excess of emission in the center of the disk for the channels between 13.1 and 14.3 km s^{-1}, seen in both ^{13}CO and C^{18}O. We will return to a discussion of a potential origin of those residuals in Section 3.4.

Motivated by the presence of the aforementioned residuals, we explored more sophisticated disk models, including a model with a vertical temperature gradient and CO depletion due to freeze-out and photodissociation (after Rosenfeld et al. 2013), as well as a flexible temperature model parameterized to mimic more sophisticated (and computationally expensive) protoplanetary disk models (Jonkheid et al. 2004; Kamp & Dullemond 2004). However, we found that neither of these models resulted in a more satisfactory fit to the data as measured by visual inspection and the Akaike information criterion (AIC; Akaike 1973). Encouragingly, however, they still yielded similar estimates of $M_{\rm tot}$ to the standard model, which gives us

confidence that the disk-based dynamical mass is sufficiently robust to the choice of parameterization for the temperature and density structures.

While the inferred physical structures inferred from each line are in mild disagreement, as might be expected for this simple parameterization, the spatial values of the inferred temperature and density in the disk are for the most part quite similar. To illustrate this, we plot the 2D temperature and density profiles inferred from each transition in Figure 5. We attribute the small differences in the structure parameters to the different layers of the disk probed by the ^{13}CO and C^{18}O transitions: the more optically thick ^{13}CO probes the upper layers of the disk atmosphere, while the more optically thin C^{18}O transition is more sensitive to the colder, denser layers of the disk midplane. In Figure 6, we plot the marginalized posteriors for both transitions in the $\{M_{\rm tot}, i_{\rm disk}\}$-plane. Interestingly, the different transitions deliver different inclinations ($\Delta i_{\rm disk} = 2°.5 \pm 1°.4$), which we attribute to the previously mentioned model deficiencies and the fact that the ^{13}CO and C^{18}O transitions probe different layers in the disk. With more computational power, it would be worthwhile to explore a joint fit to both transitions to see whether a single, more sophisticated disk structure could adequately fit both transitions simultaneously.

Nevertheless, both transitions yield consistent constraints on the total stellar mass, which is the most relevant parameter to our stated goals. The robustness of the dynamical mass technique is primarily because the kinematic morphology of the line emission (i.e., the distribution of the emission in position–velocity space) is not strongly dependent on the temperature and density structure of the disk, but is a rather strong function of $M_{\rm tot}$ and $i_{\rm disk}$. When the disk is spatially resolved, the dependence of $M_{\rm tot}$ on $i_{\rm disk}$ is considerably diminished.

We combine the inferred total masses from ^{13}CO and C^{18}O, weighted by their uncertainties, to find $M_{\rm tot} = 5.29 \pm 0.06\,M_\odot$. The uncertainty in the distance to GW Ori (388 ± 5 pc; Kounkel et al. 2017) linearly translates into a mass uncertainty, and so we convolve an additional 1.3% mass uncertainty with this posterior to arrive at $M_{\rm tot} = 5.29 \pm 0.09\,M_\odot$, which we report as the total mass estimate. Because the inferred disk inclinations are mutually inconsistent, we adopt a weighted average for the mean inclination and assume a large systematic uncertainty, resulting in a final estimate of $i_{\rm disk} = 137°.6 \pm 2°.0$. Our CO results are broadly consistent with that determined by Fang et al. (2017), who measure the disk inclination to be ~35°–40° (modulo the absolute inclination of the disk).

3.2. An Updated Model of the Stellar Orbits

In this section, we present an orbital fit to the RVs determined in Section 2.2 and then explore a joint fit to the RV data and the astrometric measurements of Berger et al. (2011). In both cases we fit a hierarchical triple model and solve for the elements of the inner and outer orbits simultaneously, assuming that the inner binary acts as a point mass in the outer orbit. To address possible systematic offsets in the RV data sets, we derive three offset terms: (1) $\Delta v^{\rm TRES}$, applied as a shift to all TRES RVs to place them on the DS reference frame; (2) $\Delta v_2^{\rm DS}$, to allow for an offset between the primary and secondary DS velocities, possibly caused by a mismatch between the template parameters and those of the true stars; and (3) $\Delta v_2^{\rm TRES}$, a similar primary/secondary offset for TRES. The residuals from our initial fit indicated that our
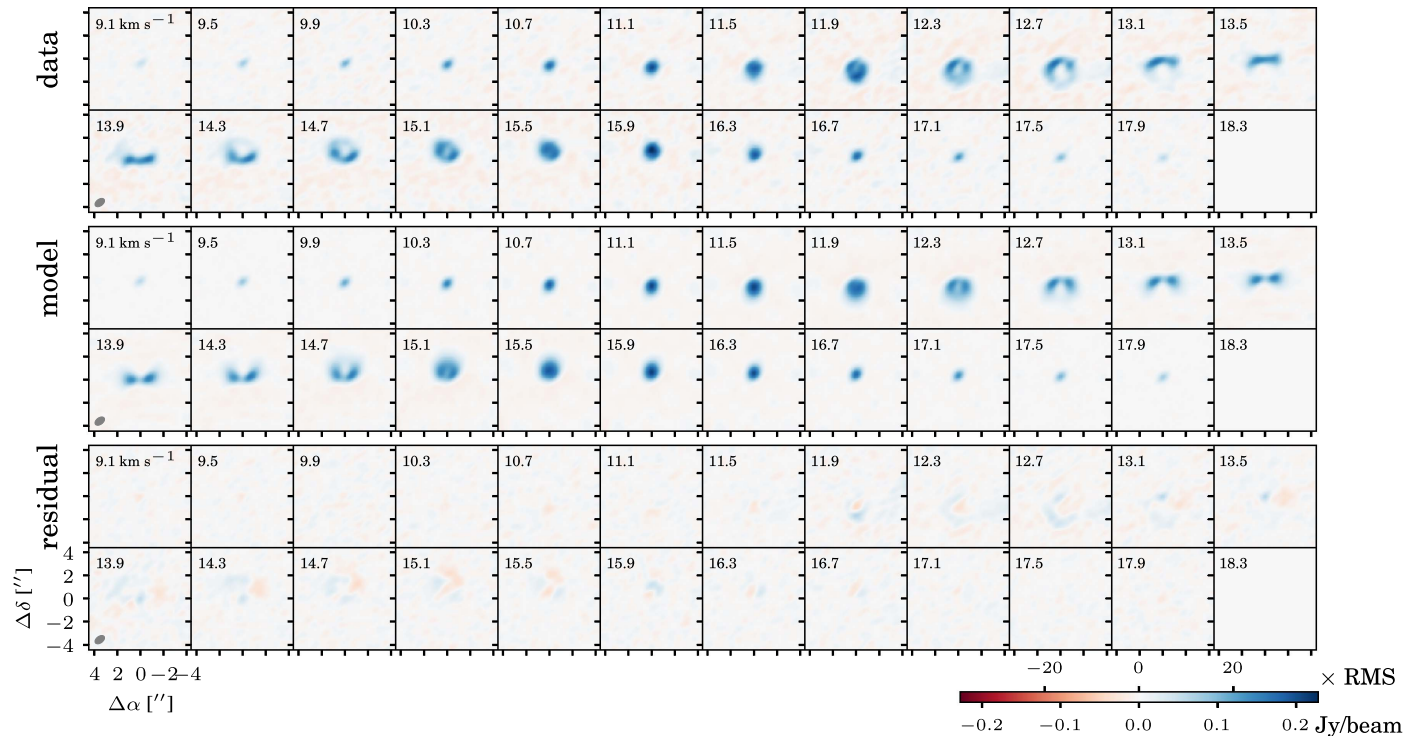
Figure 3. Comparison of the observed channel maps of the ^{13}CO line emission (top) with a best-fit model (middle; constructed from a synthetic visibility set based on the inferred parameters listed in Table 4 and then imaged in the same way as the data) and the associated residuals (bottom; the imaged data–model residual visibilities). The annotation is the same as in Figure 2.

formal velocity uncertainties are underestimated, and so the uncertainties on each measurement are scaled to achieve a reduced $\chi_\nu^2 = 1$ for our final solution.

The period of the inner orbit is consistent with that of Mathieu et al. (1991) and Fang et al. (2014); however, due to the SB2 nature of the system, most other orbital parameters are significantly different. We find a larger semiamplitude for the primary, $K_A = 8.36 \pm 0.14$ km s^{-1}, a mass ratio of $q \equiv M_B/M_A = 0.60 \pm 0.02$, and a statistically significant eccentricity $e_{\rm in} = 0.13 \pm 0.02$. The outer orbit has an orbital period of $P_{\rm out} = 4218 \pm 60$ days (11.5 yr) and a significant eccentricity, $e_{\rm out} = 0.22 \pm 0.09$. We find offset terms statistically inconsistent with zero: a small but non-negligible offset between the DS and TRES zero-points of 0.49 km s^{-1} and larger offsets for the secondary velocities of 8.77 and 6.41 km s^{-1} for the DS and TRES RVs, respectively. Given the large intrinsic line width ($v \sin i \approx 40$ km s^{-1}), these large offsets can reasonably be ascribed to template mismatch. The systemic velocity inferred from the RV fit is nicely consistent with the systemic velocity of the circumtriple disk from the ALMA data. All parameters of the RV fit are listed in the first column of Table 5. The full orbit as a function of time is shown in the second panel of Figure 7. Graphical representations of our observations and the inner and outer orbit models as a function of orbital phase are shown in Figures 8 and 9, respectively.

Although there are only three epochs of published astrometry in Berger et al. (2011), these points may still help constrain the parameter space of possible orbits. Therefore, we explore a joint RV-astrometric analysis built on a model of the "three-dimensional orbit" following Murray & Correia (2010), which adds new model parameters, including the semimajor axis, orbital inclination, and position angle of the ascending node for

both the inner and outer orbits. For a likelihood function, we combine the χ^2 RV likelihood and a new χ^2 likelihood for the angular separation and position angle measurements of the B and C components relative to A. As with the disk analysis, we also use a geometric prior on the orbital inclinations. For their last measurement epoch (2005), Berger et al. (2011) report an alternate position for the C component, and so we also perform a separate fit for this scenario.

The jointly constrained parameters are in the second and third columns of Table 5. A graphical representation of the orbit is shown in Figure 10. With the addition of the astrometric data set, we can measure the individual stellar masses and the inclinations of the orbital planes, which are also listed in Table 5. Depending on whether the original or alternate position for C is used, we find the total stellar mass to be $M_{\rm tot} = 5.7 \pm 0.7 M_\odot$ or $6.1 \pm 0.9 M_\odot$, respectively. Both measurements are consistent with the $M_{\rm tot}$ independently measured with the disk-based analysis ($M_{\rm tot} = 5.29 \pm 0.09 M_\odot$).

To measure the degree of misalignment between the orbital planes and the circumtriple disk, we calculate the angle Φ between the angular momentum vectors of each orbit according to Fekel (1981),

$$\cos \Phi = \cos i_1 \cos i_2 + \sin i_1 \sin i_2 \cos(\Omega_1 - \Omega_2). \quad (1)$$

We find that the mutual inclination between the disk and the inner orbit is $\Phi_{\rm in} = 44° \pm 5°$ and the mutual inclination between the disk and the outer orbit is $\Phi_{\rm out} = 54° \pm 7°$; these values are similar if one uses the "alternate" C position ($\Phi_{\rm in} = 45° \pm 5°$, $\Phi_{\rm out} = 50° \pm 6°$). Such a large misalignment is surprising given the naive expectation that the stellar orbits and disk would be roughly coplanar. Since these results only rest on three astrometric epochs, however, there is a possibility
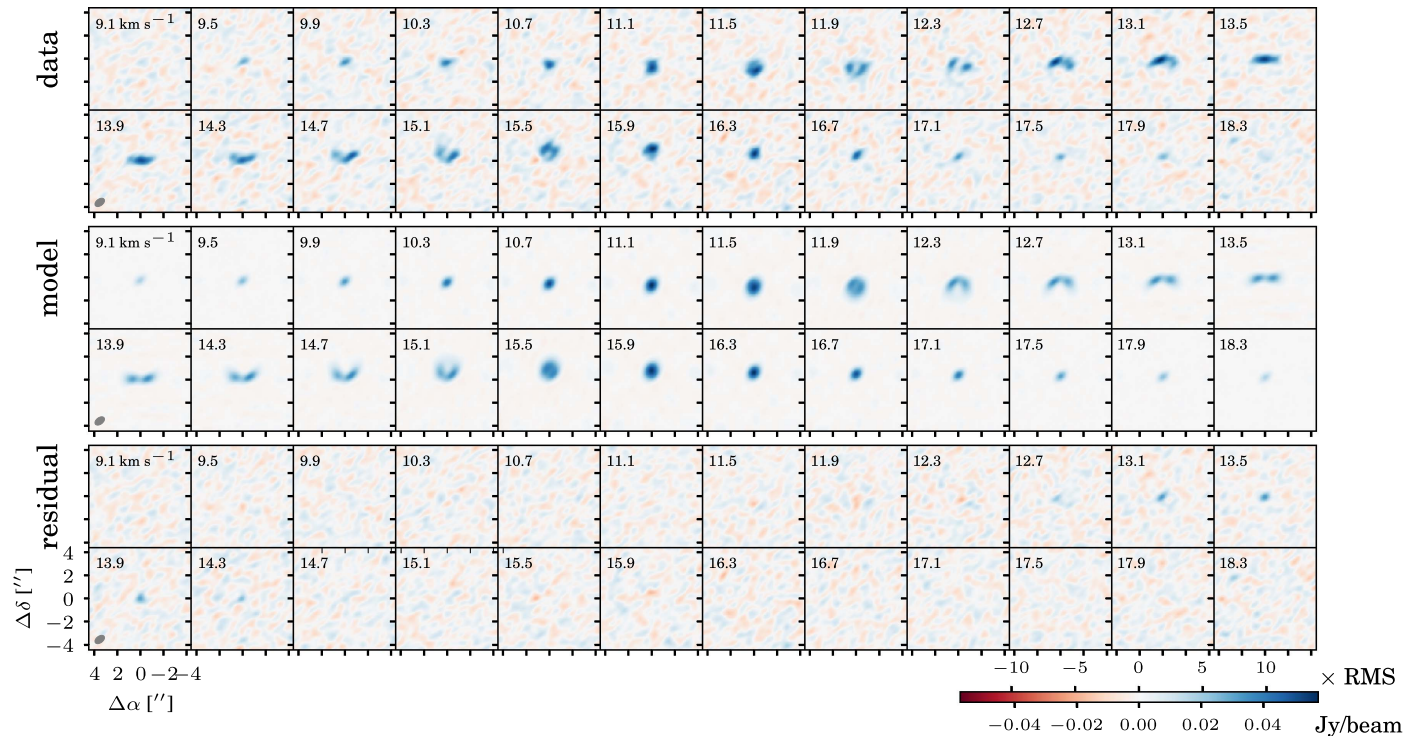
Figure 4. Comparison of the observed channel maps of the $C^{18}O$ line emission (top) with a best-fit model (middle; constructed from a synthetic visibility set based on the inferred parameters listed in Table 4 and then imaged in the same way as the data) and the associated residuals (bottom; the imaged data–model residual visibilities). The annotation is the same as in Figure 2.

that the large inferred mutual inclinations may be the result of unaccounted-for systematic effects. In the next section, we use only the newly derived RVs and disk-based dynamical mass to formulate a more conservative estimate of the mutual inclinations. We advocate continued astrometric monitoring of the GW Ori system to further improve the 3D orbit and definitively confirm the inclinations of the stellar orbits.

3.3. Joint RV + Disk Constraints on Individual Component Masses

In this section, we combine the RV analysis with the disk-based constraints on the total stellar mass to independently infer the individual stellar masses of the GW Ori system without referencing the Berger et al. (2011) astrometry. We construct a joint likelihood function with the following five parameters: M_A, M_B, M_C, i_{in}, and i_{out}. The RV constraints are sufficiently captured by the summary statistics $M_A \sin^3 i_{in}$, $M_B \sin^3 i_{in}$, $M_C \sin i_{out}/(M_{tot}/M_\odot)^{2/3}$ and the covariances between them, which are well represented by a multivariate Gaussian distribution.[18] The disk constraint on the total stellar mass M_{tot} is well represented by a Gaussian as well. We enforce flat priors on the stellar masses and geometrical priors on the inclinations. We use the ensemble sampler MCMC (Goodman & Weare 2010; Foreman-Mackey et al. 2013) with 20 walkers to explore the posterior for 50,000 iterations, burn 25,000 iterations, and assess convergence by ensuring that the Gelman–Rubin statistic (Gelman et al. 2014) is $\hat{R} < 1.1$ for all parameters.

This analysis produces consistent but less precise constraints on the stellar masses as the joint RV + astrometric fits (see Table 6). Like the RV + astrometric analysis, the disk + RV analysis also indicates that the inner stellar orbit must be significantly misaligned with the disk, although the true misalignment is unknown: the difference between i_{in} and i_{disk} only provides a lower limit on the mutual inclination because the true mutual inclination must consider the position angles of the orbits as well. To highlight these findings, we overplot our newly derived constraints on the disk inclination and the orbits in Figure 11. The measurements for the disk based on the ^{13}CO and $C^{18}O$ data indicate the lowest inclinations (nearest to edge-on, $i = 90°$). This is commensurate with the disk inclination measurements from Fang et al. (2017), and so we consider these results to be robust. Interestingly, the constraints on i_{in} differ between the RV + astrometry and the RV + disk results at a significant level. We speculate that this difference might be due to unknown systematics in the astrometry or RV data sets, or potentially an error in our assumption of the distance to GW Ori. While the astrometry + RV analysis does not require a distance to the source, the disk-based analysis does require a distance in order to break the M_{tot}/d degeneracy. Although the exact degree of mutual inclination between the inner orbit and the disk is unknown, we conclude that it is at least 10° and potentially as high as 45°.

3.4. Variability: Eclipses and Periodic Behavior

The first extensive light curve of GW Ori was published by Shevchenko et al. (1992), based on several seasons of photoelectric photometry from Maidanak Observatory. Among other modulations typical of young stars, those data revealed two deep ($\Delta V = 0.3$–0.4 mag) eclipse-like events in 1988 and 1990 (Figure 12, D and F). The span of time between these two events

---

[18] Note that we do not use additional constraints on q_{in} or other derived parameters, as this would amount to double-counting the RV constraints.
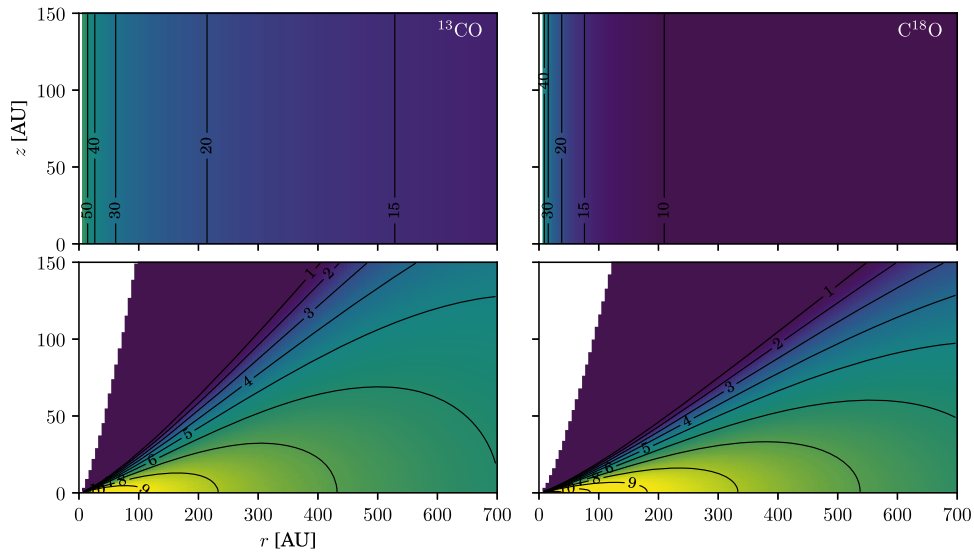
Figure 5. Maximum likelihood 2D temperature (top) and density (bottom) disk structures inferred using the ^{13}CO (left) and C^{18}O (right) transitions. The temperature contours are in units of K. The density plots show the total gas density (ρ_{gas}) and are in units of $\log_{10}$ cm^{-3}. The color scales are normalized to the same limits for both transitions.
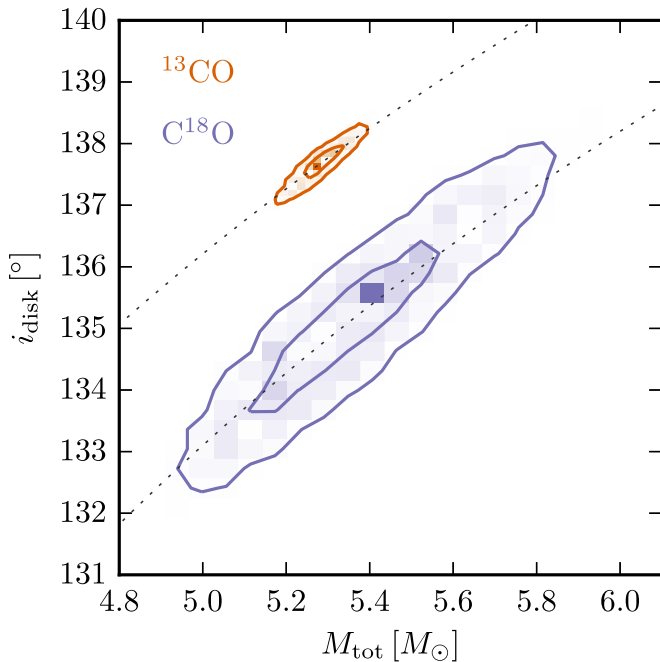
Figure 6. Posterior distributions for the model parameters fit to the ^{13}CO and C^{18}O data independently, showing 1σ and 2σ contours. Dashed lines indicate constant values of $M_{tot} \sin^2 i_{disk}$.

is exactly three orbital periods of the inner binary (the only known orbit at the time; Mathieu et al. 1991). The correlation of the eclipses with the orbital phase led to the hypothesis that these features were Algol-like fadings, where the primary is obscured by material in the overflowing Roche lobe of the secondary. For that to work, the binary orbital plane must be viewed nearly edge-on ($i_{in} \approx 90°$).

Maidanak Observatory continued their extensive photometric monitoring of GW Ori until 1996 (Shevchenko et al. 1998). Those data identified two additional eclipses, one in 1991 and one in 1992 (Figure 12, G and H), which occurred

exactly three orbital periods after the 1990 event, but with a lower amplitude ($\Delta V = 0.1$ mag). Shevchenko et al. (1998) noted that GW Ori appears to redden (in $V - R$ and $B - V$ colors) during all of these eclipses; however, insufficient precision was available to robustly constrain an associated extinction curve. Photoelectric observations by W. Herbst reveal three additional eclipses of similar depth between 1982 and 1985 (events A–C; Shevchenko et al. 1998). Those features also appear to be separated by integer multiples of the inner orbital period, lending further support to the Algol-like variable hypothesis. With their longer photometric time baseline, Shevchenko et al. (1998) also noted an overall decline of $\Delta V = 0.1$ mag in the average brightness of GW Ori from 1986 to 1991.

Given the apparent connection of these eclipse events to the orbital architecture of GW Ori, we set out to conduct a more comprehensive analysis of photometric variability in this system. We combined the complete Maidanak photometry catalog (1987–2003) with data from the ASAS, KELT, and ASAS-SN surveys to construct a light curve spanning 1987–2017. This composite light curve was manually searched for new eclipse events. Eight new eclipses were identified, bringing the total number to 15; they are listed in Table 7, marked in Figure 7, and shown in greater detail in Figure 12. Given the sometimes considerable noise in this light curve, we have only considered an event to be an eclipse if it shows multiple consecutive photometric points that deviate significantly from the running average (large dips that span only a single epoch are likely spurious). The identified eclipses are similar to the events identified by Shevchenko et al. (1992, 1998), ranging from 0.08 to 0.70 mag in depth and lasting 10–50 days.

The longer time baseline for the combined photometric catalog indicates that the eclipse events are not exclusively periodic. The 1988, 1990, and 1992 eclipses noted by Shevchenko et al. (1998) do indeed occur on integer multiples of the inner period of 241 days. However, a reanalysis of the Maidanak photometry reveals an additional likely eclipse event in 1989 (E) that is three orbital periods apart from

Table 5
Orbital Elements of GW Ori

Parameter	RV	RV + Astrometry	RV + Astrometry[a]
Inner Orbit			
P (days)	241.49 ± 0.05	241.50 ± 0.05	241.49 ± 0.04
K_A (km s^{-1})	8.36 ± 0.14	8.34 ± 0.15	8.36 ± 0.15
q	0.60 ± 0.02	0.60 ± 0.02	0.60 ± 0.02
a (au)	$\cdots$	1.25 ± 0.05	1.27 ± 0.05
e	0.13 ± 0.02	0.13 ± 0.01	0.13 ± 0.01
i (deg)	$\cdots$	157 ± 1	157 ± 1
ω_A (deg)	196 ± 7	197 ± 7	196 ± 6
Ω[c] (deg)	$\cdots$	263 ± 13	264 ± 13
T_{peri} (HJD $-2,400,000$)	56681 ± 4	56682 ± 4	56681 ± 4
γ (km s^{-1})	$+28.31 \pm 0.19$	$+28.33 \pm 0.18$	$+28.29 \pm 0.19$
Δv TRES[b] (km s^{-1})	0.49 ± 0.24	0.52 ± 0.23	0.47 ± 0.23
Δv_2 Reticon[b] (km s^{-1})	8.77 ± 0.65	8.75 ± 0.67	8.73 ± 0.66
Δv_2 TRES[b] (km s^{-1})	6.41 ± 0.37	6.36 ± 0.35	6.39 ± 0.39
M_A ($M_\odot$)	$\cdots$	$2.80^{+0.36}_{-0.31}$	$2.94^{+0.40}_{-0.40}$
M_B ($M_\odot$)	$\cdots$	$1.68^{+0.21}_{-0.18}$	$1.77^{+0.24}_{-0.24}$
Outer Orbit			
P (days)	4218 ± 60	4246 ± 66	4203 ± 60
K_{AB} (km s^{-1})	2.47 ± 0.25	2.38 ± 0.23	2.50 ± 0.24
a (au)	$\cdots$	9.19 ± 0.32	9.15 ± 0.35
e	0.22 ± 0.09	0.13 ± 0.07	0.25 ± 0.08
i (deg)	$\cdots$	150 ± 7	144 ± 9
ω_{AB} (deg)	307 ± 18	310 ± 21	310 ± 12
Ω[c] (deg)	$\cdots$	282 ± 9	263 ± 10
T_{peri} (HJD $-2,400,000$)	53560 ± 565	53911 ± 260	53878 ± 130
M_C ($M_\odot$)	$\cdots$	$1.15^{+0.40}_{-0.23}$	$0.99^{+0.35}_{-0.18}$
Derived Properties			
Inner time interval (cycles)	53.6	$\cdots$	$\cdots$
Outer time interval (cycles)	3.1	$\cdots$	$\cdots$
$M_A \sin i$ ($M_\odot$)	0.30 ± 0.02	$\cdots$	$\cdots$
$M_B \sin i$ ($M_\odot$)	0.18 ± 0.01	$\cdots$	$\cdots$
$M_C \sin i / (M_{tot}/M_\odot)^{2/3}$ ($M_\odot$)	0.22 ± 0.02	$\cdots$	$\cdots$
M_{tot} ($M_\odot$)	$\cdots$	5.7 ± 0.7	6.1 ± 0.9

Notes.
[a] Fit using the "alternate" C position for the 2005 epoch of astrometry in Berger et al. (2011).
[b] We include parameters for a potential velocity offset between the primary and secondary radial velocities for each instrument. In principle, this term should be consistent with 0; the nonzero value likely indicates that there is some moderate template mismatch between the secondary stellar spectrum and the synthetic spectrum used as a cross-correlation template.
[c] We follow the convention of the visual binary field and define the ascending node as the point where the secondary component (e.g., star B for the inner orbit, and star C for the outer orbit) crosses the plane of the sky moving *away* from the observer.

the 1991 event (G) but not at the same orbital phase as the D, F, and H events; rather, they are offset by about one-third of an orbital period. Eclipses seen in the data from the more recent surveys show a similar behavior. For example, eclipses L and M are exactly two orbital periods apart, while eclipses N and O are about a quarter period early or late. When the full light curve is phased to the inner period, as in Figure 8, the multitude of eclipse phases becomes readily apparent.

Aside from the eclipse events, the combined GW Ori light curve exhibits a striking sinusoidal variability (0.20 mag peak to trough) that is clearly phased with the outer orbital period of 11.5 yr (Figure 9). We must be careful when evaluating this oscillation mode, since it stretches across data acquired from several different instruments. Moreover, the KELT data set was not taken in *V* band; it was shifted to match the overlapping

ASAS-SN observations, meaning that it has a potentially problematic zero-point uncertainty. With these caveats in mind, the clear rising and falling trends are seen within each individual data set without the need for any vertical shifts, suggesting that this modulation is likely real. The earlier photoelectric observations of W. Herbst, stretching back to 1983, also clearly phase up with the expected sinusoidal variation. This situates the long-term dimming seen by Shevchenko et al. (1998) as part of an 11.5 yr period brightness oscillation.

When considering the phase-folded light curve on the outer (AB–C) orbital period, it appears as if the deep eclipses preferentially occur between phases 0.4 and 0.8 from periastron. However, the three eclipses in the photoelectric observations of W. Herbst fall closer to phase 0.0. Taken
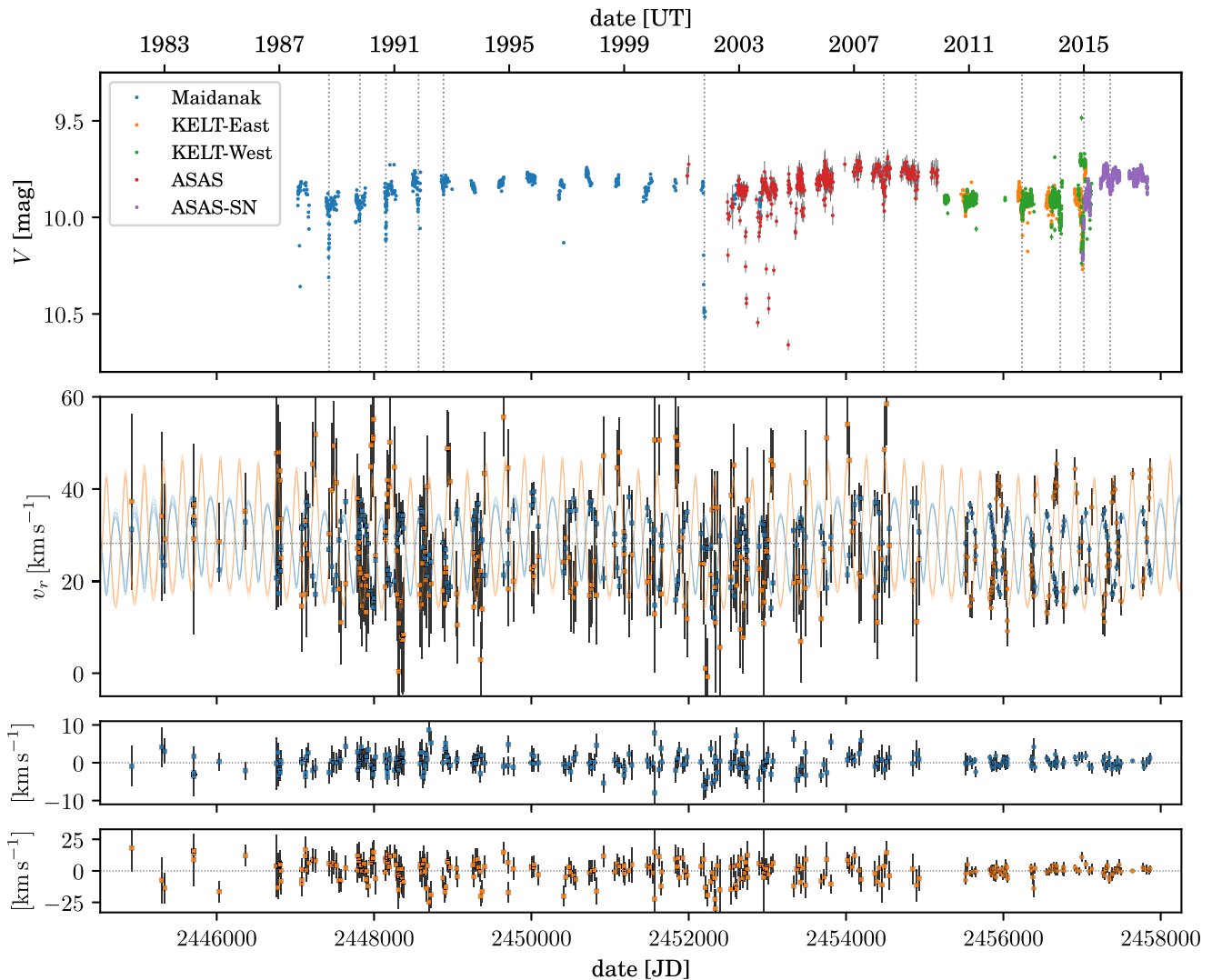
Figure 7. Top: photometric observations of GW Ori from 1987 until mid-2017. All photometric observations displayed here are in the *V* band (ASAS, ASAS-SN, and Maidanak) or a broader filter (KELT) that has been shifted to align with *V* band where the time series overlap. Bottom: primary (blue) and secondary (orange) radial velocities overlaid with several realizations of the most probable orbits, to show uncertainty in the orbit. Reticon velocities are shown with squares, TRES velocities are shown with circles, and the dotted line represents the center-of-mass velocity. Residuals for this orbit are shown in the panels below.

together, this suggests that the apparent clustering of deep eclipses could be affected by the seasonal sampling in the data set.

The 11.5 yr variability reaches a minimum flux level near apoastron (phase = 0.5) of the outer orbit. Since the light from the A–B binary dominates the total optical flux from the system, it must be one or both of these stars that are being partially occulted by circumstellar material. Due to the fact that the disk is more inclined than the stellar orbits, apoastron corresponds to the time when the A–B pair comes closest to being screened by the inner edge of the near side of the disk (see Figure 10, top right panel). From dynamical arguments, we expect the inner edge of the disk to be truncated out to 2–3 times the semimajor axis of the tertiary (Artymowicz & Lubow 1994), which corresponds to ~20–30 au in radius. Even with the foreshortening from the relative inclinations, the inner edge of the disk would not occult the A–B pair at apoastron unless the inner edge of the disk were very puffed up with a vertical extent $\gtrsim$10 au. Given the gradual dimming, it may be more likely that the A–B pair is screened by tenuous material residing inside this truncation radius, such as micron-sized dust

within the cleared region. There is circumstantial support for this interpretation from the variable infrared SED, which Fang et al. (2014) interpret as an indication of a variable reservoir of small grains near the A–B pairing that is cleared and replenished owing to the actions of the tertiary.

We find some ^{13}CO and C^{18}O emission that exceeds predictions from the most probable standard disk model at locations consistent with this near edge of the disk, but located at or near the systemic velocity (13.1–14.3 km s^{-1} LSRK). Those residuals could simply be an artifact from using an insufficiently complex disk model, but they may instead very well be probing the source of the eclipses, the long-term dimming, or both. There is an outstanding question from this analysis as to what the disk looks like on the scales of the inner orbit. The ALMA observations do not have sufficient angular resolution to probe the disk at the physical scales corresponding to the tertiary orbit, so the distribution of solids within the GW Ori disk remains relatively unconstrained. With its longest baselines, ALMA would have the spatial resolution (0″02) to probe the disk on 8 au scales, more than sufficient to

12
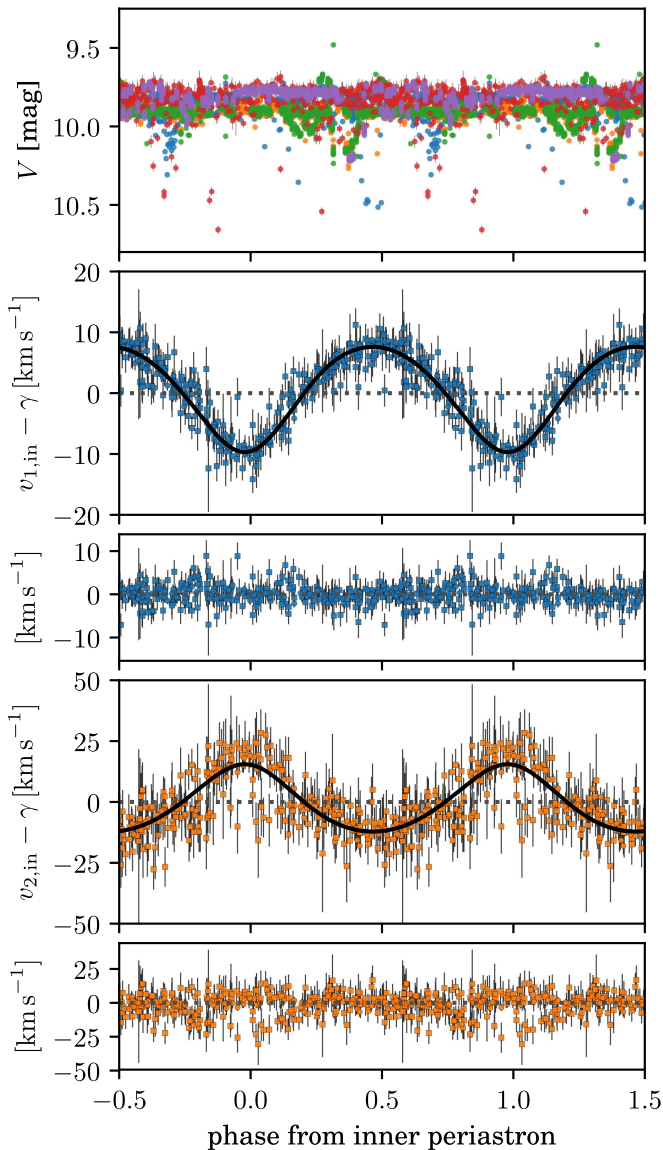
Figure 8. Top: *V*-band light curve phased to the inner orbital period. No discernible correlation is detected. The colors are the same as in the top panel of Figure 7. Bottom: RV measurements of GW Ori and the best-fit model for the inner orbit, after subtracting the motion due to the outer orbit.

Figure 9. Top: *V*-band light curve phased to the outer orbital period, showing that the mean flux level oscillates by 0.2 mag over the course of the outer orbit and is lowest during apoastron (phase 0.5). The colors are the same as in the top panel of Figure 7. Bottom: RV measurements of GW Ori and the best-fit model for the outer orbit, after subtracting the motion due to the inner orbit.

resolve a cleared region consistent with the tertiary orbit ($\gtrsim 18$ au in diameter).

Because the eclipse events are not synchronized with the outer orbital period, it is not immediately clear whether they share the same physical origin as the longer-term brightness variations. The new dynamical constraints derived earlier indicate that the A–B orbit is *not* edge-on, and so we must consider alternatives to the Algol mechanism. Any theory that seeks to explain these inner eclipses must account for several pieces of evidence, in addition to the updated orbital configuration. The eclipses span 10–50 days in duration, are of variable depth (between 0.08 and 0.70 mag), appear to be consistent with reddening by dust, are not strictly periodic with the inner period, and seem to occur at all phases of the outer orbital period. Moreover, the spectra (unwittingly) taken during times of eclipse show no obvious changes in spectral features beyond the normal variability described by Fang et al. (2014). We speculate that these quasi-periodic eclipses may be due to

an unstable circumbinary disk around A–B, or possibly the result of eclipses of A by accretion streams onto the individual circumstellar disks of either A or B.

Finally, we searched for additional periodicity in the light curve beyond the inner and outer orbital periods. After excluding eclipses, we used the Lomb–Scargle (LS) periodicity search algorithm (Lomb 1976; Scargle 1982) within the VARTOOLS analysis package (Hartman & Bakos 2016) to search for periodic modulations from 1.1 to 100 days in the high-cadence KELT data set. The most significant period we recover is 2.93 ± 0.05 days, shown in Figure 13. We suggest that this corresponds to the rotation period of the primary, although we note that Bouvier (1990) and Fang et al. (2014) derived alternate rotation periods of 3.3 days and 5.0–6.7 days, respectively. Future high-precision, high-cadence observations of GW Ori will help to unambiguously identify the rotation period of A.
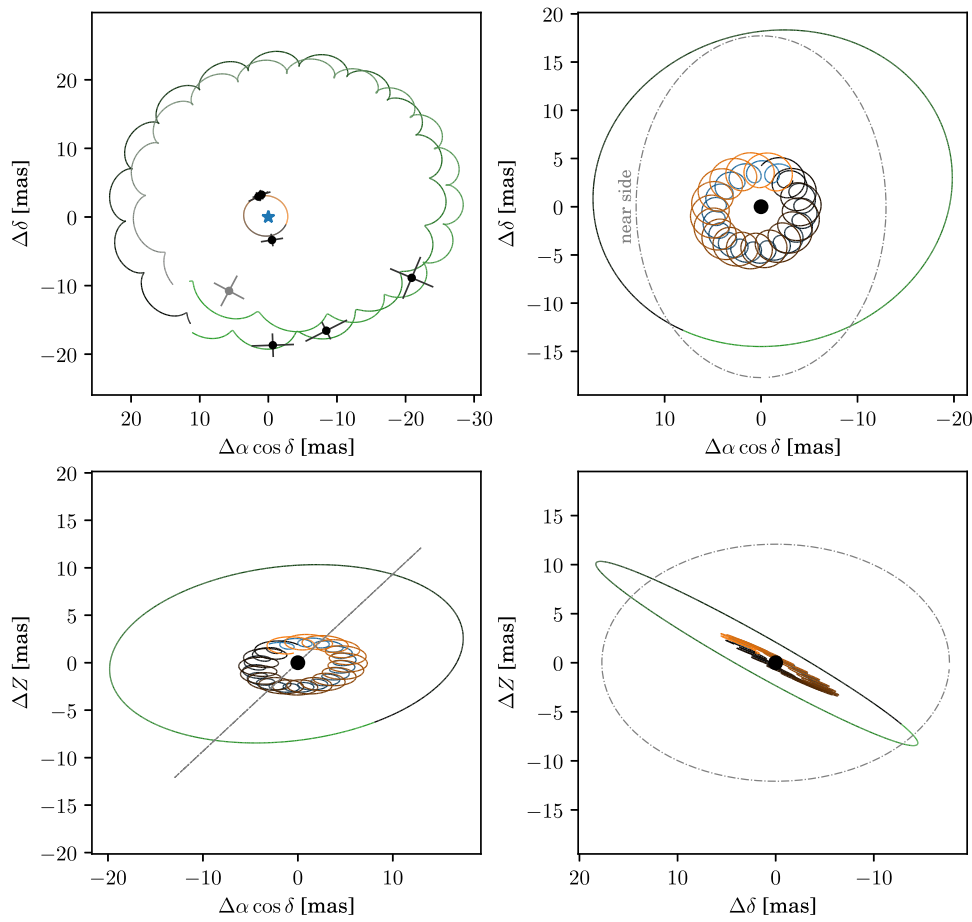
Figure 10. Orbits from the joint RV-astrometric fit shaded according to their phase, where black represents periastron and color hue increases with orbital phase. Top left: orbits relative to the primary star A, in the plane of the sky, with the three epochs of astrometry from Berger et al. (2011). The light-gray data point and outer orbit represent the fit to the "alternate" position for C. The following three plots are relative to the center of mass of the system. A fictitious particle at 7 au on a circular orbit coplanar with the circumtriple disk is shown as a gray dashed line. Top right: sky plane. For future discussion in Section 3.4, we label the side of the disk nearest to the observer. Bottom left: looking down the north axis. Bottom right: looking down the east axis. Positive Z points toward the observer.

Table 6
Joint Constraints on Stellar Masses and Orbital Inclinations

Parameter	RV + Astrometry	RV + Disk
M_A ($M_\odot$)	$2.80^{+0.36}_{-0.31}$	$2.74^{+0.15}_{-0.52}$
M_B ($M_\odot$)	$1.68^{+0.21}_{-0.18}$	$1.65^{+0.10}_{-0.31}$
M_C ($M_\odot$)	$1.15^{+0.40}_{-0.23}$	$0.88^{+0.85}_{-0.19}$
i_{in} (deg)	157^{+1}_{-1}	151^{+1}_{-2}
i_{out} (deg)	150^{+7}_{-7}	130^{+28}_{-27}

Note. The RV + astrometry values are replicated from Table 5 for comparison purposes. We note that we are not able to infer the absolute inclination of the stellar orbits directly from the radial velocity data, so there are in fact alternate solutions for the RV + disk results that yield $i_{alt} = 180° − i$. These solutions would be inconsistent with the astrometric motion, however, so we opt to only report the solutions with $i \geqslant 90°$.

4. Discussion

With the newly derived component masses now established, we turn to discussion of the photospheric properties of the stars and the age of the GW Ori system. With these in place, we discuss the system architecture in the context of other multiple systems.
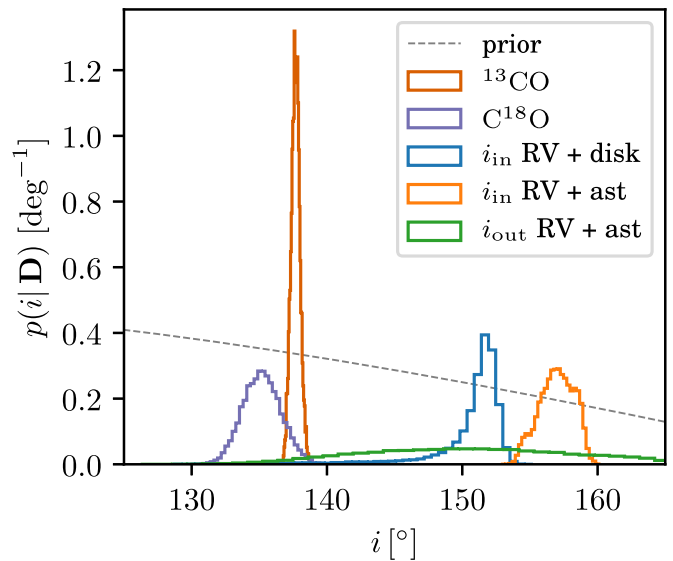
Figure 11. Inclination posteriors on the disk inclination, inner stellar orbit, and outer stellar orbit, as determined from various joint fits. Because i_{out} is essentially unconstrained by the RV + disk analysis, it is not plotted for aesthetic reasons. The geometric prior on inclination (uniform orientation of orbits in 3D space) is shown as a thin gray dotted line.
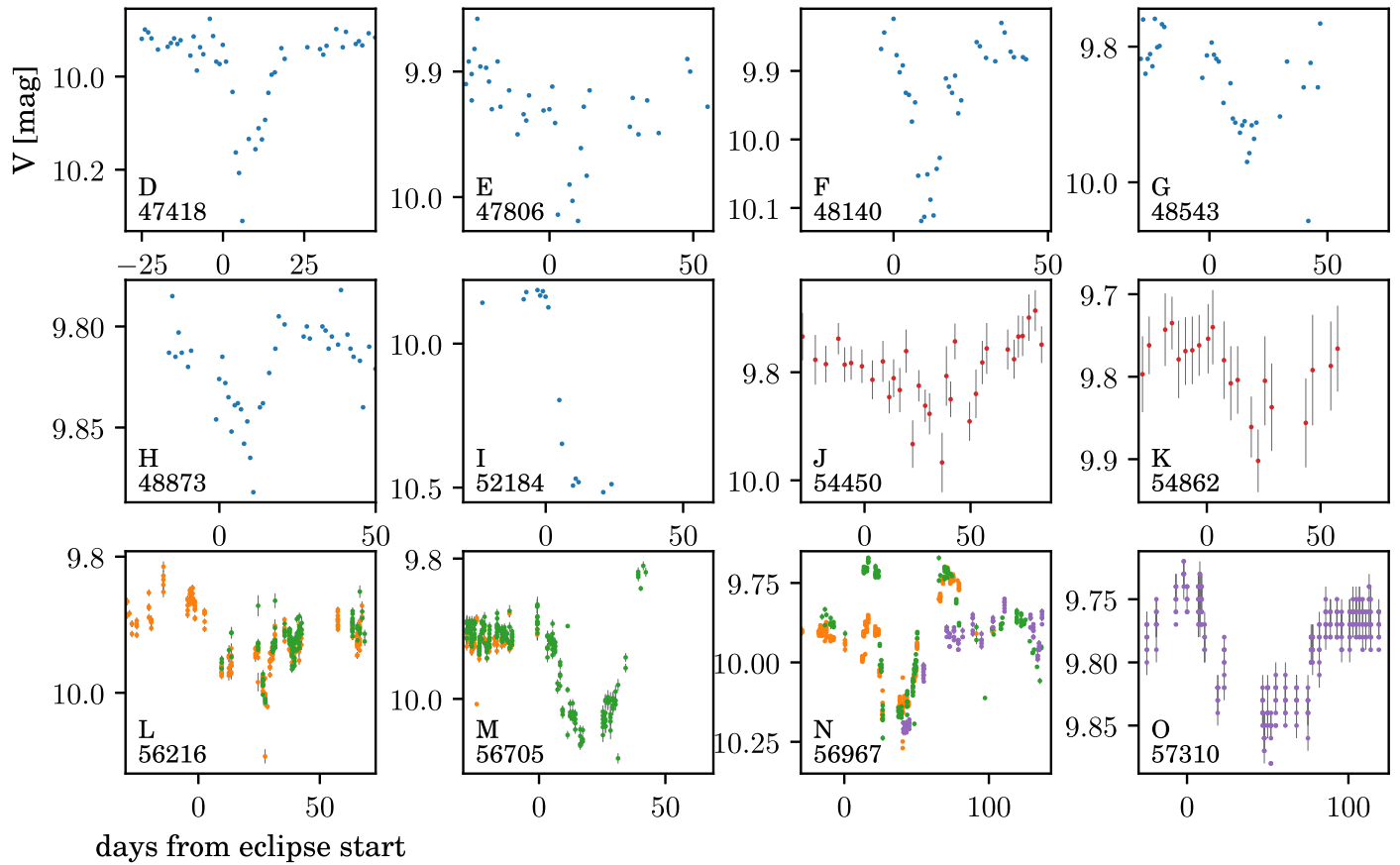
Figure 12. Gallery of the eclipse events noted in Table 7, labeled relative to the start of the eclipse. The colors are the same as in the top panel of Figure 7. Note that the *y*-axis scale is significantly different from panel to panel, with some eclipses as deep as 0.7 mag and others less than 0.1 mag.

4.1. Age and Photospheric Properties

In order to place GW Ori A and GW Ori B on the H-R diagram, we require updated measurements of their luminosities. To obtain those, we assembled an SED of GW Ori from the same sources listed in Fang et al. (2014), i.e., the $UBVR_CI_C$ photometry from Calvet et al. (2004) and the JHK_s photometry from the Two Micron All Sky Survey (2MASS; Skrutskie et al. 2006). We then manually adjusted the 2MASS *J* and *H* fluxes down by 5% and 10%, respectively, to account for the approximate contamination in those bands from star C based on the flux ratios from Berger et al. (2011). We fitted the SED using a two-component model based on the NextGen atmospheres (Hauschildt et al. 1999) and the Cardelli et al. (1989) reddening law with the following constraints: distance to the source of 388 ± 5 pc, spectroscopically determined flux ratio at 5187 Å of 0.25 ± 0.05, primary T_{eff} of 5700 ± 200 K, and *H*-band flux ratio $f_B/f_A = 0.57 \pm 0.05$ (Berger et al. 2011). That analysis yields an extinction of $A_V = 1.2 \pm 0.2$ mag, secondary $T_{eff} = 4900 \pm 200$ K, luminosities of $L_A = 32.5 \pm 5.0\,L_\odot$ and $L_B = 12.8 \pm 2.4\,L_\odot$, radii of $R_A = 5.90 \pm 0.18\,R_\odot$ and $R_B = 5.01 \pm 0.22\,R_\odot$, and a *V*-band flux ratio of 0.33 ± 0.04.

Figure 14 places the GW Ori A and B stars on the H-R diagram, along with some representative stellar evolutionary tracks from the MIST models (Choi et al. 2016). The mass tracks start at $0.5\,M_\odot$ and increase in increments of $0.5\,M_\odot$; the isochrones are at ages of 0.1, 0.5, 1.0, 2.0, and 3.0 Myr. The positions of A and B in this diagram are consistent with their

measured dynamical masses at ages of 0.3–1.3 Myr. However, the evolutionary tracks would imply that the A component is older than the B component by at least 0.3 Myr. This age discrepancy is likely not real, but rather the result of inaccuracies in the photospheric properties, evolutionary models, or both. The revised mass for GW Ori A is significantly lower than previous estimates in the literature (Berger et al. 2011; Fang et al. 2014), which, combined with the revised photospheric properties, means that the age of GW Ori is now slightly older than was previously implied. Even with its lower mass and luminosity, however, it is still true that GW Ori A is a Herbig Ae/Be precursor (as was also noted by Fang et al. 2014) and will evolve to a main-sequence (MS) late B/early A star.
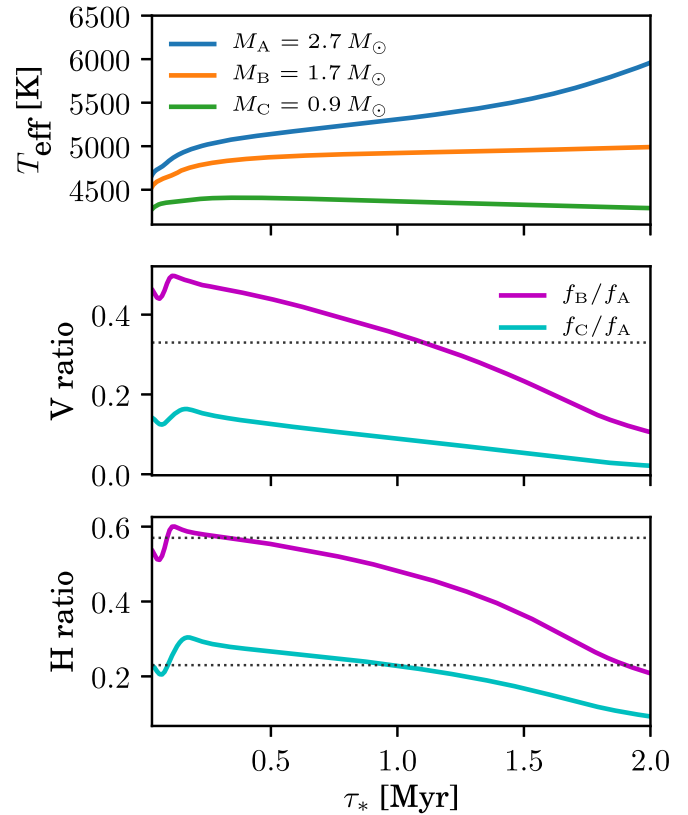
In Figure 15, we utilize the three MIST models nearest the best-fit masses for each of the stellar components to compute the evolution of the effective temperatures and the *V*- and *H*-band flux ratios, and we compare these quantities with the existing photospheric measurements. Beyond the primary and secondary effective temperatures and *V*-band flux ratio reported in this work, there are two *H*-band flux ratio constraints from Berger et al. (2011), $f_B/f_A = 0.57 \pm 0.05$ and $f_C/f_A = 0.23 \pm 0.01$ (computed as the weighted mean of all three of their epochs). In general, the measured effective temperatures and flux ratios agree well with the predictions from the models in the age range 0.3–1.3 Myr. The predicted *V*-band flux contribution for the C component is very small ($\lesssim 5\%$ of the total flux), explaining why we were unable to find optical
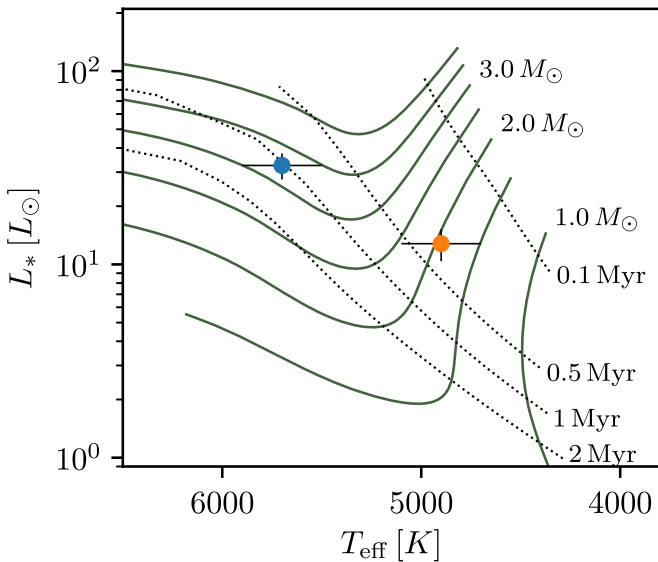
Table 7
V-band Photometric Eclipse Catalog

Label	UT Mid	Start (JD)	End (JD)	Duration (days)	Depth (mag)	Telescope
A	1982 Oct	⋯	⋯	⋯	⋯	Herbst
B	1983 May	⋯	⋯	⋯	⋯	Herbst
C	1984 Nov	⋯	⋯	⋯	⋯	Herbst
D	1988 Sep 13	2,447,418	2,447,435	17	0.40	Maidanak
E	1989 Oct 6	2,447,806	2,447,833	27	0.10	Maidanak
F	1990 Sep 5	2,448,140	2,448,161	21	0.35	Maidanak
G	1991 Oct 13	2,448,543	2,448,589	46	0.15	Maidanak
H	1992 Sep 7	2,448,873	2,448,893	20	0.08	Maidanak
I	2001 Oct 1	2,452,184	$\geqslant$2,452,215	$\geqslant$31	0.70	Maidanak
J	2007 Dec 15	2,454,450	2,454,508	58	0.10	ASAS
K	2009 Jan 30	2,454,862	2,454,912	50	0.15	ASAS
L	2012 Oct 15	2,456,216	2,456,259	43	0.11	KELT
M	2014 Feb 16	2,456,705	2,456,744	39	0.20	KELT
N	2014 Nov 5	2,456,967	2,457,080	30–130	0.25	KELT/ASAS-SN
O	2015 Oct 14	2,457,310	2,457,405	95	0.10	ASAS-SN
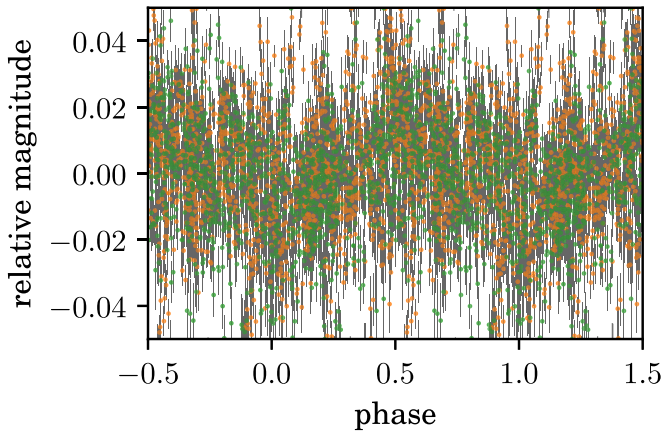
Figure 13. KELT photometric observations of GW Ori, with the three eclipses removed, phased to the 2.93-day period recovered from our LS analysis. Legend as in Figure 7.

Figure 14. GW Ori A and B placed on the PMS H-R diagram, with evolutionary tracks from Choi et al. (2016). Mass tracks are in increments of 0.5 $M_\odot$ from 1.0 to 4.0 $M_\odot$, and isochrones label ages of 0.1, 0.5, 1, and 2 Myr.

Figure 15. Relative photospheric properties of the GW Ori stellar components as a function of age, using the MIST PMS evolutionary models and assuming that the stars are coeval. The measured effective temperatures for the primary and secondary ($T_{\rm eff} = 5700 \pm 200$ K and $T_{\rm eff} = 4900 \pm 200$ K, respectively), the *V*-band flux ratio ($f_{\rm B}/f_{\rm A} = 0.33 \pm 0.04$), and the *H*-band flux ratios ($f_{\rm B}/f_{\rm A} = 0.57 \pm 0.05$ and $f_{\rm C}/f_{\rm A} = 0.23 \pm 0.01$; Berger et al. 2011) are shown here as dotted lines and are all roughly consistent with the model predictions for ages of 0.3–1.3 Myr.

spectroscopic signatures of this component even though it is nearly a solar-mass star.

As noted by Berger et al. (2011), it is possible that one, two, or all three of the stars might show excess *H*-band emission

owing to the presence of a circumstellar disk and/or accretion signatures above the photospheric emission of these stars. While we find that the measured photospheric properties are reasonably consistent without invoking such an excess, there is circumstantial evidence for the idea (beyond the eclipses). Najita et al. (2003) found blended CO fundamental emission peaks, which Bast et al. (2011) suggested might actually be the blended profiles of emission originating from physically distinct regions, e.g., individual circumstellar disks around the A and B stars. However, it may also be possible that the CO fundamental emission originates from the inner edge of the circumtriple disk, cleared by the ∼9 au orbit of the tertiary (C).

Assuming that the 2.93-day period identified in the KELT photometry corresponds to the rotation period of the primary, we can use the inferred primary radius and the spectroscopic measurement of the rotational line broadening ($v \sin i_A$) to infer its stellar obliquity, modulo its absolute orientation. Solving for the inclination and propagating the uncertainties in the respective parameters yields an obliquity of $i_A = 23° \pm 3°$, which is in remarkable agreement (modulo the absolute orientation) with the inclination of the inner stellar orbit ($157° \pm 1°$) as determined from the RV + astrometry analysis (Section 3.3).

4.2. The GW Ori Triple System in Context

The many unique data sets presented in this paper have enabled us to paint a detailed picture of the GW Ori system. It is young (0.3–1.3 Myr), contains a considerable amount of stellar mass ($M_{tot} = 5.29 \pm 0.09 \, M_\odot$), and hosts a massive disk ($M_{disk} \approx 0.1 \, M_\odot$), which makes it an extremely interesting system to study in the context of theories about star and planet formation, migration, and stability.

We estimated the total disk mass of GW Ori using the results from our ^{13}CO and $C^{18}O$ modeling in Section 3.1, which we emphasize are very indirect measurements that rely on uncertain conversion factors between ^{12}CO and H_2. We find somewhat larger disk masses when modeling $C^{18}O$ compared to ^{13}CO (0.095 $M_\odot$ versus 0.020 $M_\odot$, respectively), which is in conflict with the finding of Fang et al. (2017) that $C^{18}O$ must be depleted relative to ^{13}CO. We attribute the differences in our disk masses to insufficiently complex models of disk structure and optical depth effects and note that in general estimating disk masses from CO is notoriously difficult (Yu et al. 2017), although in our case it is encouraging that they are roughly consistent with estimates based on the dust continuum emission (0.1 $M_\odot$; Fang et al. 2017). In the context of the large disk mass survey by Andrews et al. (2013), GW Ori's disk mass is slightly larger than the mean predicted value for its stellar mass, although still consistent with the large 1σ envelope in this relationship at high stellar masses. In light of this large disk mass, we investigate whether the disk is Toomre stable today. We use the more massive M_{disk} values from the $C^{18}O$ results to derive a lower bound on Toomre's Q parameter:

$$Q(r) = \frac{c_s \Omega}{\pi G \Sigma} = \sqrt{\frac{k_B M_{tot}}{\pi^2 \mu m_H G}} \sqrt{\frac{T(r)}{r^2 \Sigma^2(r)}}. \tag{2}$$

For the range of disk parameters determined from our CO fitting, the minimum value is $Q \approx 100$ at $r \sim 300$ au, which means that the disk is not currently undergoing a global gravitational instability ($Q \approx 1$).

Now we turn to a brief discussion of relevant analogs to the GW Ori system. There are now at least four circumbinary disks known around short-period (10–20 days) eccentric binaries: UZ Tau E, V4046 Sgr, AK Sco, and DQ Tau (Jensen et al. 2007; Rosenfeld et al. 2012; Czekala et al. 2015b, 2016, and references therein). All four systems have their binary orbital plane and associated circumbinary disk aligned to within 3°. These findings agree well with the low mutual inclinations found for *Kepler* circumbinary planets (Winn & Fabrycky 2015) and therefore have exciting implications for a large circumbinary planet occurrence rate (Li et al. 2016). Of course, severe selection effects are at work in both samples, and so care must be taken when extrapolating these results to the population at large. Within this context, GW Ori stands apart owing to the fact that its stellar orbit is *not* aligned with the disk. This may be a consequence of the larger stellar masses involved, the longer orbital period(s), and/or the existence of a close tertiary. Here we examine several other longer-period systems that are characterized by their significantly nonzero mutual inclinations and show that the large mutual inclinations found in GW Ori are not as unique when considering other longer-period systems.

KH 15D is an eccentric ($e = 0.6$) binary system with a slightly longer period than the aforementioned systems (48 days) and hosts a circumbinary dust ring misaligned by 10°–20° from the stellar orbit (Chiang & Murray-Clay 2004; Capelo et al. 2012). The eccentric stellar orbit and disk misalignment cause dramatic photometric eclipse events, as stars are screened by the edge of the dust disk. The eclipses also come and go as the ring precesses about the binary. The edge of the occulting disk must be sharp, suggesting that the ring is confined to a narrow region by a planet at 4 au. The disk and stellar orbital misalignment may be driven by dynamical interactions between the eccentric binary and the disk (e.g., Martin & Lubow 2017; Zanazzi & Lai 2018).

Moving to still larger orbital separations, the frequency of disk–stellar orbital alignment becomes less clear, mainly due to incomplete orbital coverage. Consider GG Tau A, which is a triple system with circumstellar disks around each of the three components, as well as a larger circumtriple disk. The circumtriple disk is composed of a dense ring containing 80% of the mass and an outer gas disk extending up to 800 au, and it is of similar mass to that of the GW Ori disk (0.12 $M_\odot$; Guilloteau et al. 1999). The stellar architecture of GG Tau A is rather different from that of GW Ori, however. The primary star Aa has a mass of 0.78 $M_\odot$ and is situated in an "outer" orbit with another binary, Ab1–Ab2, which together have a combined mass of less than 0.7 $M_\odot$ (Dutrey et al. 2016). The orbital elements of the triple system still have some uncertainty. Nelson & Marzari (2016) make a dynamical argument that the outer orbit has a semimajor axis of 62 au and is likely coplanar with the outer circumtriple ring; on the other hand, Cazzoletti et al. (2017) argue from disk dynamics that the disk and binary planes are misaligned by 20°–30°. Further astrometric observations are required to definitively characterize this system.

Recently, the transition disk system HD 142527 ($M_* = 2.0 \, M_\odot$, $M_{disk} \sim 0.1 \, M_\odot$) was discovered to have an M dwarf companion orbiting inside its large disk cavity (Biller et al. 2012; Lacour et al. 2016). The presence of this companion provides a possible explanation for why a smaller, inner disk in this system appears to be highly misaligned

($\sim 70°$; Avenhaus et al. 2014; Marino et al. 2015), which may be driven by secular precession resonance between the disk and the companion (Owen & Lai 2017). The extreme mass ratio between the M dwarf and the primary ($q = 0.05$–0.10) puts the HD 142527 system in a different class of multiple-star systems than those considered so far. Even though the system parameters do not map directly to sources like GW Ori, these dynamical effects are still important to consider, especially since most existing observations do not have sufficient sensitivity to detect such small companions for most sources (GW Ori included).

At younger ages, the Class I binary system L1551 IRS 5 is an interesting analog because it hosts a large circumbinary disk ($r \sim 500$ au, $M_{disk} \approx 0.07\,M_\odot$; Eisner 2012; Takakuwa et al. 2017) outside of two circumstellar disks. The binary is on a wide orbit ($a = 70$ au), to which the circumstellar disks are misaligned by up to $25°$. The relative proper motion of the binary over a 15 yr baseline indicates that it contains $1.7\,M_\odot$ of stellar mass on a 246 yr orbit (Villa et al. 2017). The circumstellar disks are probably aligned with the rotation of the outer circumbinary envelope, which may indicate that the stars were formed by rotationally driven fragmentation, preserving this orientation (Lim et al. 2016).

The most recent example of a misaligned circumbinary disk is in the TWA 3A system (Kellogg et al. 2017), which hosts a circumbinary disk within a hierarchical triple system of stars of near equal mass (spectral types M3–M4). The "inner" binary Aa–Ab has a 35-day eccentric ($e = 0.63$) orbit and hosts a small disk extending 25 au in size (Andrews et al. 2010), while the "outer" orbit A–B takes 200–800 yr. Although the absolute inclinations are not yet known, the parameter space is sufficiently constrained such that it is likely that all three planes (the inner orbit, outer orbit, and cirumbinary disk) are misaligned by at least $30°$. The Aa–Ab circumbinary disk mutual inclination may be attributable to torques from the distant B companion.

Of all these T Tauri sources surveyed, GW Ori stands out in terms of stellar mass. Its architecture proved relatively difficult to probe via traditional detection techniques, requiring sustained, long-term RV monitoring over 35 yr, as well as sophisticated care and attention to derive an RV solution for the blended line profiles. Finally, resolved submillimeter interferometric observations were necessary to measure the inclination of the circumtriple disk. Looking forward, sustained campaigns of astrometric monitoring will be most helpful for definitively constraining the orbital inclinations.

Although there may still be significant dynamical evolution in the architecture of the GW Ori system before it reaches the MS, it is also worth briefly considering how its orbital parameters compare to the general MS population of triple stars, even though this population of older systems may have experienced significant dynamical evolution. Among late B star primaries (of which GW Ori A will be on the MS), 13% of systems have multiplicity of three or higher (Eggleton & Tokovinin 2008); this fraction is roughly constant across spectral types B–G. In a detailed analysis of higher-order multiple systems, Tokovinin (1997) found that the ratio P_{long}/P_{short} was greater than 10 in almost all systems, presumably reflecting which orbits are stable. While GW Ori's ratio (17) is smaller than most, it is not an outlier among triple systems. Tokovinin (1997, 2017) finds that the distribution of mutual inclinations between the orbital planes in triple systems

is inconsistent both with complete alignment of the inner and outer orbits (zero mutual inclination), as well as completely independent inclinations (randomly distributed). For triples with outer projected separation <50 au the average misalignment is $20°$, while orbits wider than 1000 au are not preferentially aligned. The RV + astrometric fits for GW Ori suggest that the stellar orbits are consistent with this picture (a mutual inclintion of $13° \pm 6°$). The population of misaligned triples may be the result of accretion of gas with randomly aligned angular momentum at the epoch of star formation.

Like most multiple stars, those in GW Ori likely formed through turbulent fragmentation of the molecular cloud, possibly at larger separations than they are now, and then hardened through decay via dynamical interactions, accretion, and the interaction of the circumstellar disks (Offner et al. 2010; Bate 2012). Continued study of the GW Ori system, including spatially resolving the innermost regions to discover circumstellar disks and their relative inclinations, will be valuable to further understanding its formation process.

5. Summary and Conclusions

In this work we performed the following:

1. Used spatially and spectrally resolved ALMA observations of the GW Ori circumtriple disk to derive a dynamical mass of $M_{tot} = 5.29 \pm 0.09\,M_\odot$. We find that the disk is large, massive, and inclined at $i_{disk} = 137°.6 \pm 2°.0$.

2. Used 35 yr of high-resolution optical spectra to derive new radial velocities for both components in the inner binary. We then fit a hierarchical triple orbit and found a 241-day inner period (A–B) and an 11.5 yr outer period (AB–C). When we combined the RV constraints with the disk-based constraint on M_{tot}, we found stellar masses of $M_A = 2.7\,M_\odot$, $M_B = 1.7\,M_\odot$, and $M_C = 0.9\,M_\odot$, to a precision of $\pm 0.3\,M_\odot$.

3. Combined the RV data with the astrometric data from Berger et al. (2011) to perform a joint RV-astrometric fit and found large mutual inclinations between the stellar orbits and the disk ($\Phi_{in} = 44° \pm 5°$, $\Phi_{out} = 54° \pm 7°$). The stellar orbits may be mildly misaligned with each other ($\Phi_{in/out} = 13° \pm 6°$).

4. Placed GW Ori A and B on the H-R diagram and found that their stellar properties are broadly consistent with the predictions of PMS models for their measured masses at an age of ≈ 1 Myr.

5. Compiled a light curve with a 30 yr baseline and identified several new eclipse events. We also identified a 0.2 mag amplitude mode of variability phased with the outer orbital period, which suggests that the A–B binary may be partially obscured by micron-sized grains in the circumtriple disk cavity at outer apoastron.

6. Placed GW Ori in the context of other PMS multiple systems. While short-period eccentric binary systems generally seem to have low mutual inclinations with their circumbinary disks, there are a number of longer-period systems that exhibit significant mutual inclinations.

Given its uniquely large stellar mass, massive circumtriple disk, and puzzling eclipse behavior, GW Ori should remain a high-priority target to study a unique class of dynamical interactions in PMS multiple systems.

ORCID iDs

Ian Czekala ● https://orcid.org/0000-0002-1483-8811
Sean M. Andrews ● https://orcid.org/0000-0003-2253-2270
Guillermo Torres ● https://orcid.org/0000-0002-5286-0251
Joseph E. Rodriguez ● https://orcid.org/0000-0001-8812-0565
Keivan G. Stassun ● https://orcid.org/0000-0002-3481-9052
David W. Latham ● https://orcid.org/0000-0001-9911-7388
David J. Wilner ● https://orcid.org/0000-0003-1526-7587
Michael A. Gully-Santiago ● https://orcid.org/0000-0002-4020-3457
Michael B. Lund ● https://orcid.org/0000-0003-2527-1598
Robert J. Siverd ● https://orcid.org/0000-0001-5016-3359
B. Scott Gaudi ● https://orcid.org/0000-0003-0395-9869
Benjamin J. Shappee ● https://orcid.org/0000-0003-4631-1149
Thomas W.-S. Holoien ● https://orcid.org/0000-0001-9206-3460

References

Akaike, H. 1973, in Proc. 2nd Int. Symp. on Information Theory, ed. B. N. Petrov & F. Caski (Budapest: Akadémiai Kiadó), 267
Andrews, S. M., Czekala, I., Wilner, D. J., et al. 2010, ApJ, 710, 462
Andrews, S. M., Rosenfeld, K. A., Kraus, A. L., & Wilner, D. J. 2013, ApJ, 771, 129
Artymowicz, P., & Lubow, S. H. 1994, ApJ, 421, 651
Astropy Collaboration, Robitaille, T. P., Tollerud, E. J., et al. 2013, A&A, 558, A33
Avenhaus, H., Quanz, S. P., Schmid, H. M., et al. 2014, ApJ, 781, 87
Bast, J. E., Brown, J. M., Herczeg, G. J., van Dishoeck, E. F., & Pontoppidan, K. M. 2011, A&A, 527, A119
Bate, M. R. 2012, MNRAS, 419, 3115
Berger, J.-P., Monnier, J. D., Millan-Gabet, R., et al. 2011, A&A, 529, L1
Bezanson, J., Edelman, A., Karpinski, S., & Shah, V. B. 2017, SIAMR, 59, 65
Biller, B., Lacour, S., Juhász, A., et al. 2012, ApJL, 753, L38
Bouvier, J. 1990, AJ, 99, 946

Brown, T. M., Baliber, N., Bianco, F. B., et al. 2013, PASP, 125, 1031
Buchhave, L. A., Bakos, G. Á, Hartman, J. D., et al. 2010, ApJ, 720, 1118
Calvet, N., Muzerolle, J., Briceño, C., et al. 2004, AJ, 128, 1294
Capelo, H. L., Herbst, W., Leggett, S. K., Hamilton, C. M., & Johnson, J. A. 2012, ApJL, 757, L18
Cardelli, J. A., Clayton, G. C., & Mathis, J. S. 1989, ApJ, 345, 245
Cazzoletti, P., Ricci, L., Birnstiel, T., & Lodato, G. 2017, A&A, 599, A102
Chiang, E. I., & Murray-Clay, R. A. 2004, ApJ, 607, 913
Choi, J., Dotter, A., Conroy, C., et al. 2016, ApJ, 823, 102
Czekala, I., Andrews, S. M., Jensen, E. L. N., et al. 2015a, ApJ, 806, 154
Czekala, I., Andrews, S. M., Mandel, K. S., Hogg, D. W., & Green, G. M. 2015b, ApJ, 812, 128
Czekala, I., Andrews, S. M., Torres, G., et al. 2016, ApJ, 818, 156
Czekala, I., Mandel, K. S., Andrews, S. M., et al. 2017, ApJ, 840, 49
Dolan, C. J. 2000, PhD thesis, Univ. Wisconsin-Madison
Dolan, C. J., & Mathieu, R. D. 2001, AJ, 121, 2124
Dolan, C. J., & Mathieu, R. D. 2002, AJ, 123, 387
Duchêne, G., & Kraus, A. 2013, ARA&A, 51, 269
Dullemond, C. P. 2012, RADMC-3D: A Multi-purpose Radiative Transfer Tool, Astrophysics Source Code Library, ascl:1202.015
Dutrey, A., Di Folco, E., Beck, T., & Guilloteau, S. 2016, A&ARv, 24, 5
Eggleton, P. P., & Tokovinin, A. A. 2008, MNRAS, 389, 869
Eisner, J. A. 2012, ApJ, 755, 23
Fang, M., Sicilia-Aguilar, A., Roccatagliata, V., et al. 2014, A&A, 570, A118
Fang, M., Sicilia-Aguilar, A., Wilner, D., et al. 2017, A&A, 603, A132
Fekel, F. C., Jr. 1981, ApJ, 246, 879
Foreman-Mackey, D., Hogg, D. W., Lang, D., & Goodman, J. 2013, PASP, 125, 306
Fűrész, G. 2008, PhD thesis, Univ. Szeged
Gaia Collaboration, Brown, A. G. A., Vallenari, A., et al. 2016, A&A, 595, A2
Gelman, A., Carlin, J. B., Stern, H. S., et al. 2014, Bayesian Data Analysis, Vol. 2 (Boca Raton, FL: CRC Press)
Goodman, J., & Weare, J. 2010, Communications in Applied Mathematics and Computational Science, 5, 65
Guilloteau, S., Dutrey, A., & Simon, M. 1999, A&A, 348, 570
Hartman, J. D., & Bakos, G. Á 2016, A&C, 17, 1
Hartmann, L., Calvet, N., Gullbring, E., & D'Alessio, P. 1998, ApJ, 495, 385
Hauschildt, P. H., Allard, F., Ferguson, J., Baron, E., & Alexander, D. R. 1999, ApJ, 525, 871
Henkel, C., Wilson, T. L., Langer, N., Chin, Y.-N., & Mauersberger, R. 1994, in The Structure and Content of Molecular Clouds, ed. T. L. Wilson & K. J. Johnston (Berlin: Springer), 72
Husser, T.-O., Wende-von Berg, S., Dreizler, S., et al. 2013, A&A, 553, A6
Jensen, E. L. N., Dhital, S., Stassun, K. G., et al. 2007, AJ, 134, 241
Jonkheid, B., Faas, F. G. A., van Zadelhoff, G.-J., & van Dishoeck, E. F. 2004, A&A, 428, 511
Kamp, I., & Dullemond, C. P. 2004, ApJ, 615, 991
Kellogg, K., Prato, L., Torres, G., et al. 2017, ApJ, 844, 168
Kochanek, C. S., Shappee, B. J., Stanek, K. Z., et al. 2017, PASP, 129, 104502
Kounkel, M., Hartmann, L., Loinard, L., et al. 2017, ApJ, 834, 142
Kuhn, R. B., Rodriguez, J. E., Collins, K. A., et al. 2016, MNRAS, 459, 4281
Kurtz, M. J., & Mink, D. J. 1998, PASP, 110, 934
Lacour, S., Biller, B., Cheetham, A., et al. 2016, A&A, 590, A90
Latham, D. W. 1992, in ASP Conf. Ser. 32, IAU Colloq. 135: Complementary Approaches to Double and Multiple Star Research, ed. H. A. McAlister & W. I. Hartkopf (San Francisco, CA: ASP), 110
Li, G., Holman, M. J., & Tao, M. 2016, ApJ, 831, 96
Lim, J., Yeung, P. K. H., Hanawa, T., et al. 2016, ApJ, 826, 153
Lomb, N. R. 1976, Ap&SS, 39, 447
Lynden-Bell, D., & Pringle, J. E. 1974, MNRAS, 168, 603
Marino, S., Perez, S., & Casassus, S. 2015, ApJL, 798, L44
Martin, R. G., & Lubow, S. H. 2017, ApJL, 835, L28
Mathieu, R. D., Adams, F. C., Fuller, G. A., et al. 1995, AJ, 109, 2655
Mathieu, R. D., Adams, F. C., & Latham, D. W. 1991, AJ, 101, 2184
McMullin, J. P., Waters, B., Schiebel, D., Young, W., & Golap, K. 2007, in ASP Conf. Ser. 376, Astronomical Data Analysis Software and Systems XVI, ed. R. A. Shaw, F. Hill, & D. J. Bell (San Francisco, CA: ASP), 127
Murray, C. D., & Correia, A. C. M. 2010, in Exoplanets, ed. S. Seager (Tucson, AZ: Univ. of Arizona Press), 15
Najita, J., Carr, J. S., & Mathieu, R. D. 2003, ApJ, 589, 931
Nelson, A. F., & Marzari, F. 2016, ApJ, 827, 93
Offner, S. S. R., Kratter, K. M., Matzner, C. D., Krumholz, M. R., & Klein, R. I. 2010, ApJ, 725, 1485
Owen, J. E., & Lai, D. 2017, MNRAS, 469, 2834

Prantzos, N., Aubert, O., & Audouze, J. 1996, A&A, 309, 760
Prato, L., Ruiz-Rodriguez, D., & Wasserman, L. 2017, eprint (arXiv:1711.09449)
Rosenfeld, K. A., Andrews, S. M., Hughes, A. M., Wilner, D. J., & Qi, C. 2013, ApJ, 774, 16
Rosenfeld, K. A., Andrews, S. M., Wilner, D. J., & Stempels, H. C. 2012, ApJ, 759, 119
Scargle, J. D. 1982, ApJ, 263, 835
Shappee, B. J., Prieto, J. L., Grupe, D., et al. 2014, ApJ, 788, 48
Shevchenko, V. S., Grankin, K. N., Ibragimov, M. A., & Melnikov, S. Y. 1992, IBVS, 3746, 1
Shevchenko, V. S., Grankin, K. N., Ibragimov, M. A., Mel'Nikov, S. Y., & Yakubov, S. D. 1993, Ap&SS, 202, 121
Shevchenko, V. S., Grankin, K. N., Mel'Nikov, S. Y., & Lamzin, S. A. 1998, AstL, 24, 528
Simon, M., Dutrey, A., & Guilloteau, S. 2000, ApJ, 545, 1034
Simon, M., Guilloteau, S., Di Folco, E., et al. 2017, ApJ, 844, 158
Siverd, R. J., Beatty, T. G., Pepper, J., et al. 2012, ApJ, 761, 123
Skrutskie, M. F., Cutri, R. M., Stiening, R., et al. 2006, AJ, 131, 1163
Stassun, K. G., Feiden, G. A., & Torres, G. 2014, NewAR, 60, 1
Takakuwa, S., Saigo, K., Matsumoto, T., et al. 2017, ApJ, 837, 86
Tody, D. 1986, Proc. SPIE, 627, 733
Tody, D. 1993, in ASP Conf. Ser. 52, Astronomical Data Analysis Software and Systems II, ed. R. J. Hanisch, R. J. V. Brissenden, & J. Barnes (San Francisco, CA: ASP), 173
Tokovinin, A. 2017, ApJ, 844, 103
Tokovinin, A. A. 1997, A&AS, 124, 75
Torres, G., Neuhäuser, R., & Guenther, E. W. 2002, AJ, 123, 1701
Villa, A. M., Trinidad, M. A., de la Fuente, E., & Rodríguez-Esnard, T. 2017, RMxAA, 53, 525
Winn, J. N., & Fabrycky, D. C. 2015, ARA&A, 53, 409
Yu, M., Evans, N. J., II, Dodson-Robinson, S. E., Willacy, K., & Turner, N. J. 2017, ApJ, 841, 39
Zanazzi, J. J., & Lai, D. 2018, MNRAS, 473, 603